Contributions of mirror-image hair cell orientation to mouse otolith organ and zebrafish neuromast function

Kazuya Ono[#1], Amandine Jarysta[#2], Natasha C. Hughes[#3], Alma Jukic[#4], Hui Ho Vanessa Chang[3], Michael R. Deans[5,6], Ruth Anne Eatock[*1], Kathleen E. Cullen[*3,7,8,9], Katie Kindt[*4] and Basile Tarchini[*2,10]

[1] Department of Neurobiology, University of Chicago, Chicago, IL, 60637, USA.
[2] The Jackson Laboratory, Bar Harbor, ME 04609, USA.
[3] Dept. of Biomedical Engineering, Johns Hopkins University, Baltimore, 21205 MD, USA
[4] Section on Sensory Cell Development and Function, National Institute on Deafness and Other Communication Disorders, National Institutes of Health, Bethesda, MA, USA
[5] Department of Neurobiology, Spencer Fox Eccles School of Medicine, University of Utah, Salt Lake City, Utah, USA.
[6] Department of Otolaryngology - Head & Neck Surgery, Spencer Fox Eccles School of Medicine at the University of Utah, Salt Lake City, Utah, USA.
[7] Department of Otolaryngology-Head and Neck Surgery, Johns Hopkins University, Baltimore 21205 MD, USA.
[8] Department of Neuroscience, Johns Hopkins University, Baltimore 21205 MD, USA.
[9] Kavli Neuroscience Discovery Institute, Johns Hopkins University, Baltimore 21205 MD, USA.
[10] Tufts University School of Medicine, Boston, MA 02111, USA.

[#] co-first authors
[*] Corresponding authors

SUMMARY/ABSTRACT

Otolith organs in the inner ear and neuromasts in the fish lateral-line harbor two populations of hair cells oriented to detect stimuli in opposing directions. The underlying mechanism is highly conserved: the transcription factor EMX2 is regionally expressed in just one hair cell population and acts through the receptor GPR156 to reverse cell orientation relative to the other population. In mouse and zebrafish, loss of Emx2 results in sensory organs that harbor only one hair cell orientation and are not innervated properly. In zebrafish, Emx2 also confers hair cells with reduced mechanosensory properties. Here, we leverage mouse and zebrafish models lacking GPR156 to determine how detecting stimuli of opposing directions serves vestibular function, and whether GPR156 has other roles besides orienting hair cells. We find that otolith organs in *Gpr156* mouse mutants have normal zonal organization and normal type I-II hair cell distribution and mechano-electrical transduction properties. In contrast, *gpr156* zebrafish mutants lack the smaller mechanically-evoked signals that characterize Emx2-positive hair cells. Loss of GPR156 does not affect orientation-selectivity of afferents in mouse utricle or zebrafish neuromasts. Consistent with normal otolith organ anatomy and afferent selectivity, *Gpr156* mutant mice do not show overt vestibular dysfunction. Instead, performance on two tests that engage otolith organs is significantly altered – swimming and off-vertical-axis rotation. We conclude that GPR156 relays hair cell orientation and transduction information downstream of EMX2, but not selectivity for direction-specific afferents. These results clarify how molecular mechanisms that confer bi-directionality to sensory organs contribute to function, from single hair cell physiology to animal behavior.

INTRODUCTION

The vestibular system provides essential information about the head's motion and orientation relative to gravity and plays a vital role in everyday life. Fundamental gaps exist in our understanding of vestibular development and function. For example, we do not fully understand how the abrupt reversal of hair cell (HC) orientation in otolith organs affects vestibular function, and whether the reversal also impacts HC mechano-electrical transduction properties or afferent neuron contacts. We explore these questions further in mouse and in the zebrafish lateral line, a sensory system where external fluid flow is detected by neuromast organs that also feature HC reversal.

Vestibular HCs reside in five sensory organs per inner ear in human, mouse and larval zebrafish: three cristae ampullaris and two otolith (or macular) organs. Within each of these organs, HCs are precisely oriented to detect mechanical stimuli based on direction. HCs are sensitive to the proportion of a stimulus aligned with the mechanosensory hair bundle's orientation: a vector from the bundle's short edge to its tall (kinociliary) edge. In cristae, which detect angular head motions, HCs are oriented uniformly to detect fluid flow in the plane of the attached semicircular canal. In contrast, HCs in otolith organs are oriented to respond to a range of head positions and linear motions in an approximately horizontal (utricle) or vertical (saccule) plane (Fig. 1A). Within these planes, HCs show two opposing orientations across a virtual "line of polarity reversal" (LPR), a conserved anatomical feature in all otolith organs (Denman-Johnson and Forge, 1999; Flock, 1964; Lindeman, 1969). HCs are also aligned in two opposing orientations in fish and amphibian neuromasts in the lateral-line system. Orientation reversal confers on neighboring HCs of opposing orientations opposite responses to the same local stimulus: depolarization and increased afferent spike rate in one population, but hyperpolarization and decreased spike rate in the other. This functional prediction and its utility are well established in neuromasts as the ability to sensitively detect water movements in two directions (Chitnis et al., 2012; Lopez-Schier et al., 2004). Beyond increasing the range of stimulus orientations detected, it remains unclear how HCs with opposing orientations and responses serve otolith organ function.

In the utricle, the LPR also segregates distinct zones, for example the lateral extrastriola (LES) from the more medial striola (Fig. 1A). Zones are strikingly different regions found in all vestibular epithelia, with ‘central’ and ‘peripheral’ zones of cristae corresponding to striolar and extrastriolar zones of maculae, respectively. Afferents that innervate striolar HCs have irregular spike timing and adapting responses in contrast to afferents that innervate extrastriolar HCs which have more regular and tonic spikes (Goldberg, 1991; Goldberg, 2000). Striolar afferents transmit more information about the time course of translational self-motion, while extrastriolar afferents better discriminate between different static head orientations relative to gravity (Jamali et al., 2019). Correlated with these physiological differences between zones are differences in HCs and afferent morphologies. Both the striola and extrastriola are populated by type I HCs contacted by *calyx afferent endings* and type II HCs contacted by *bouton afferent endings.* Most individual afferents in both zones contact both type I and type II HCs (“*dimorphic afferents*”). However, pure-calyx and pure-bouton individual afferents are respectively only found in the striola and extrastriola (Eatock and Songer, 2011; Goldberg, 2000). In amniotes there is no obligatory relationship between HC orientation reversal and zones. While the utricular striola is entirely medial to the LPR, the saccular striola is bisected by the LPR (Fig. 1A) (Deans, 2013; Li et al., 2008; Xue and Peterson, 2006). Moreover, central and peripheral zones of cristae bear many anatomical and physiological similarities to the striolar and extrastriolar zones, but cristae have no LPR and no abrupt variation in HC orientation, as in the organ of Corti.

Interestingly, mammalian otolith afferents have two distinct anatomical properties that segregate with the LPR. First, individual afferents are maximally excited by stimuli of one orientation and not the opposite (Fernandez et al., 1972; Goldberg et al., 1990), indicating that individual afferents selectively contact HCs sharing the same general orientation, as also observed in the zebrafish lateral line (Ji et al., 2018). Second, the central projections of afferent neurons innervating HCs on each side of the LPR are also distinct; afferents that innervate one HC orientation largely project to the cerebellum, while the opposite HC orientation projects to the brainstem (Ji et al., 2022; Maklad et al., 2010). The LPR thus

correlates with a striking segregation of both the peripheral and central projections of afferent neurons.

Recent work has illuminated how HCs with opposing orientations are formed during development (reviewed in (Tarchini, 2021)). Early in development all organs are polarized by core PCP proteins that are enriched asymmetrically at cell-cell junctions before HCs are born (Deans, 2013). In cristae, asymmetric core PCP proteins set up a default, uniform HC orientation across the epithelium. Because the asymmetric pattern of core PCP protein enrichment is unchanged across the LPR, a distinct, regional mechanism defines a HC population with an opposite orientation (Deans, 2013; Deans et al., 2007; Jones et al., 2014; Mirkovic et al., 2012). Regional expression of the transcription factor EMX2 in the lateral utricle and posterior saccule drives the 180°-reversed orientation of HCs compared to neighboring *Emx2*-negative HCs (Holley et al., 2010; Jiang et al., 2017). Although regionally restricted, *Emx2* is expressed by all cell types in the sensory epithelium. Reversal is achieved cell-autonomously in HCs by an orphan GPCR, GPR156 (Kindt et al., 2021). Unlike *Emx2*, *Gpr156* is transcribed throughout the sensory epithelia but is limited to HCs. In *Emx2*-positive HCs only, the GPR156 protein is trafficked and planar-polarized at apical junctions, where it signals through inhibitory G proteins to trigger a reversal in HC orientation. The EMX2>GPR156 reversal cascade is conserved in zebrafish neuromasts and loss of either of these proteins produces neuromasts where all HCs adopt the same, uniform orientation (Jacobo et al., 2019; Jiang et al., 2017; Kindt et al., 2021; Kozak et al., 2020; Lozano-Ortega et al., 2018).

Importantly, in addition to reversing HC orientation, Emx2 is required for afferent selectivity. In zebrafish *emx2* mutants, individual afferent fibers either innervate nearly all or very few HCs instead of innervating ~50% of HCs based on their shared orientation (Ji et al., 2018). In mouse otolith organs, regional *Emx2* expression is required for local afferents that innervate HC of one orientation to project centrally to the cerebellum and not to the brainstem (Ji et al., 2022). In zebrafish, Emx2 was also recently shown to affect HC mechanotransduction, thus defining an orientation-based functional asymmetry in lateral-line neuromasts (Chou et al., 2017; Kindig et al., 2023). It remains unknown

whether, similar to Emx2, GPR156 is required for orientation-based selectivity of afferent contacts in mouse otolith organs or zebrafish neuromasts, and whether Gpr156 participates in direction-based asymmetry of mechanosensitive response in neuromasts.

Here, using animal models where *Gpr156* is inactivated, we first established that abolishing the LPR in mouse otolith organs did not produce obvious changes in HC patterning and mechanotransduction properties. In contrast, we found that similar to Emx2, Gpr156 is required for asymmetric mechanotransduction in zebrafish neuromasts. Normal afferent segregation was maintained in both mice and zebrafish lacking GPR156 despite one HC population failing to reverse its orientation. Unchanged afferent organization in the mouse allowed us to specifically interrogate how the LPR serves vestibular function. We found that although *Gpr156* mutant mice did not show overt vestibular dysfunction, performance on two tests that engage otolith organs was significantly altered. This study clarifies how molecular mechanisms that orient HCs to achieve bi-directional sensitivity contribute to vestibular and lateral-line function.

170 **RESULTS**

171

172 **Normal hair cell numbers and organization in *Gpr156* mutant adult otolith organs**

173

174 In previous work (Kindt et al., 2021), we established that in sensory organs of the inner
175 ear and lateral-line, *Gpr156* expression is limited to HCs. In neonate otolith organs, we
176 demonstrated that GPR156 is required for EMX2-positive HCs to adopt a reversed
177 orientation compared to EMX2-negative HCs. We further showed that EMX2-positive HCs
178 lacking GPR156 do not correct their orientation with time and remain non-reversed in
179 young adults (P21-P28). Focusing on the utricular sensory epithelium, we showed normal
180 macular surface area and number of HCs in all three zones (LES, striola and MES; Fig.
181 1A) in adult *Gpr156*$^{del/del}$ mutants. Here we begin by extending our morphological
182 characterization of *Gpr156*$^{del/del}$ adult macular organs to include the saccule as well as
183 zonal and HC type profiles, before proceeding to functional and behavioral assessments.

184

185 We first verified that absence of GPR156 did not obviously interfere with striolar patterning
186 in adult animals. We used oncomodulin (OCM) to immunolabel striolar HCs (Simmons et
187 al., 2010) at 4-week of age (P28) and confirmed that striolar surface area and striolar HC
188 density were unaffected in constitutive *Gpr156*$^{del/del}$ mutant utricles and saccules
189 compared to controls (*Gpr156*$^{del/+}$; Fig. 1B-C). Each macular organ contains two main HC
190 types, type I and type II. Therefore, we next quantified type I HCs in the LES, striola and
191 MES zones of the adult utricle and in the anterior (ANT), striolar and posterior (POST)
192 zones of the adult saccule. We used SPP1/Osteopontin, a marker that labels the neck
193 region of approximately 90% of type I HCs (Fig. 1D-E) (McInturff et al., 2018). We
194 observed no difference in SPP1-positive type I HC numbers between mutants and
195 controls in any zone or organ (Fig. 1F). We next used a SOX2 antibody to label type II
196 HCs in the same zones (Fig. 1G-H). Again, we observed no difference in type II HC
197 numbers between mutants and controls (Fig. 1I). In summary, loss of GPR156 prevents
198 *Emx2*-positive HCs from reversing their orientation but does not affect macular patterning,
199 including division into clear zones and appropriate numbers of type I and type II HCs
200 throughout.

201

202 **No defects in mechano-electrical transduction were detected in individual mouse**
203 **utricular hair cells of *Gpr156* mutants**

204

205 *Gpr156* inactivation could be a powerful model to specifically ask how HC reversal
206 contributes to vestibular function. However, GPR156 may have other confounding roles
207 in HCs besides regulating their orientation, similar to EMX2, which impacts
208 mechanotransduction in zebrafish HCs (Kindig et al., 2023) and afferent innervation in
209 mouse and zebrafish HCs (Ji et al., 2022; Ji et al., 2018). After establishing normal
210 numbers and types of mouse vestibular HCs, we thus first assessed whether HCs
211 respond normally to hair bundle deflections in the absence of GPR156. For this
212 assessment, we recorded whole-cell mechano-electrical transduction (MET) currents of
213 HCs in the utricle of *Gpr156*$^{del/del}$ mutants. To stimulate transduction, we deflected
214 individual mechanosensory hair bundles of HCs from *Gpr156*$^{del/del}$ mutants and
215 heterozygous *Gpr156*$^{del/+}$ control utricles with a rigid probe coupled to the back (short
216 edge) of the bundle (see Methods, Fig. 2A). All bundles were positively deflected along
217 their orientation axes. I_{MET} recordings were taken between P8 and P100 (median age for
218 comparisons: ~P20 for both null and heterozygous genotypes; see Tables).

219

220 We first compared properties of the evoked MET current (I_{MET}) across genotypes in the
221 LES, the zone in which hair bundles fail to reverse in *Gpr156* mutants. ~70% (93/135) of
222 LES HCs responded with detectable I_{MET} (within 20 pA) to hair bundle deflection,
223 regardless of HC type and genotype (Chi-squared test, Table 1). We attribute the
224 insensitivity of the remaining cells to damage during dissection of the tissue, given that
225 damaged bundles can be seen in every preparation, zone, and bundle type, independent
226 of genotype.

227

228 I_{MET} responses are shown for families of iterated 400-ms steps of displacement; subsets
229 of these families are shown in Fig. 2B-E. During bundle displacement, I_{MET} typically
230 peaked at step onset. As noted before (Vollrath and Eatock, 2003), traces evoked by
231 stimuli in the middle of the operating range adapted with a time course fit by 1-2 decaying

232 exponential terms. Because type I and II HCs were voltage-clamped at different holding
233 potentials (V_{hold} = –94 and –84 mV, respectively, see Methods), their MET currents
234 experienced different driving forces. We normalized for driving force by converting current
235 to conductance (G) and plotted G as a function of hair bundle displacement (X) for each
236 HC type and genotype (Fig. 2F-G). G(X) curves were fit with a simple Boltzmann function
237 (Eq. 1, Methods), yielding values for maximum conductance (G_{max}), the midpoint of the
238 G(X) curve ($X_{1/2}$, displacement at half-maximal I_{MET}) and *dx* (slope factor), the
239 displacement range corresponding to an e-fold increase in G for small displacements.
240 Among the LES HCs tested, no significant differences were detected between genotypes
241 for any Boltzmann parameter (G_{max}, $X_{1/2}$, or *dx*) (Fig. 2F-G, Table 2). G_{max} values were in
242 the range of 2.5-3.0 nS, $X_{1/2}$ was 200-300 nm and *dx* was 150-200 nm (Table 2). From
243 G(X) relations we estimated the operating range (OR; displacement range yielding 10-
244 90% growth of G_{MET}) to be ~800-900 nm for all LES HCs (Table 2). In summary, the peak
245 (non-adapted) displacement sensitivity of I_{MET} was not detectably affected in LES hair
246 bundles of mutants.
247
248 Another salient feature of vestibular HC transduction is adaptation (response decay)
249 during a steady hair bundle deflection. We fit the adaptation with one or more exponential
250 decays, and also calculated its extent (% decay) (Eq. 4, Methods; Fig. 2B-E). As reported
251 previously for immature mouse utricular HCs (Vollrath and Eatock, 2003), these mature
252 mouse utricular HCs had fast and slow adaptation components. The fast component was
253 more prominent at small displacements and the slow component dominated at large
254 displacements; often, both were evident in the middle of the operating range. We
255 therefore compared adaptation time constants, τ_{fast} and τ_{slow}, at the midpoint of the
256 operating range ($X_{1/2}$). For 400-ms steps, mean values are in the range of 4 - 10 ms and
257 70 – 140 ms, respectively, and the two components are responsible for comparable
258 extents of the total adaptation. These results are consistent with previous reports with
259 similar methods from immature mouse utricular HCs (Vollrath and Eatock, 2003) and
260 immature rat saccular HCs (Songer and Eatock, 2013. In the current sample, however,
261 adaptation at $X_{1/2}$ included a significant third, faster adaptation component ("very fast";

262 τ_{VF} < 1 ms) in most type I HCs (12/13) and 2/10 type II HCs. In the LES, we detected no
263 significant differences with genotype in adaptation rates or extent (Table 2).
264
265 **No changes were detected in voltage-gated conductances of individual mouse**
266 **utricular hair cells of *Gpr156* mutants**
267
268 MET current initiates the receptor potential, which in turn modulates substantial voltage-
269 gated currents in the HC's basolateral membrane, especially K^+ currents, which further
270 shape the receptor potential. For example, type I HCs make relatively fast, small receptor
271 potentials compared to type II HCs because type I HCs have many more K channels that
272 are open around resting potential. To test for effects of *Gpr156* deletion on voltage-
273 dependent currents, we applied voltage step protocols to whole-cell clamped type I and
274 type II HCs in the LES of *Gpr156*$^{del/del}$ and *Gpr156*$^{del/+}$ utricles (Fig. 3A-D).
275
276 The time course and voltage dependence of outwardly rectifying voltage-gated current
277 from LES type I cells of *Gpr156*$^{del/del}$ utricles resembled those of *Gpr156*$^{del/+}$ utricles (Fig.
278 3A, C). Most of the current in type I HCs (Fig. 3A, C) flows through a low-voltage-activated
279 K^+ conductance ($g_{K,L}$) that dominates the type I HC voltage response. As described in
280 Methods, we used the current data to generate conductance density vs. voltage (G/Cm -
281 V) curves (Fig. 3E) and fitted them with the Boltzmann function (Eq. 5, Methods) to show
282 how the open probability of $g_{K,L}$ varies with voltage. In both genotypes, approximately half
283 of $g_{K,L}$ was activated at resting membrane potential, V_{rest} (~–85 mV). As a consequence
284 of their large K^+ conductance at V_{rest}, type I cells had low input resistances (R_{in} ~50 MΩ).
285 As is typical of type I HCs, the maximal K^+ conductance density (G_{max}/C_m), which is
286 proportional to the maximal number of open channels per unit membrane area, was much
287 larger than for type II HCs (Fig. 3E vs. 3F, note difference in conductance scale; Table 3).
288
289 Similarly, we detected no effect of genotype on the voltage-dependent outward currents
290 of LES type II HCs (Fig. 3B, D, F). The currents activated positive to resting potential (~–
291 72 mV) and had activation midpoints ($V_{1/2}$ values) of –30 to –40 mV. Because of the small
292 voltage-gated conductance at rest, input resistance was ~10-fold higher than in type I

293 HCs (~500 MΩ vs. ~50 MΩ). The outward currents inactivated significantly within 400 ms,
294 indicating a substantial A-current component. The maximum conductance density
295 (G_{max}/C_m) at 400 ms (~steady state), which is proportional to the number of open channels
296 per unit membrane area, was much smaller than in type I HCs. Again, no effect of
297 genotype was detected on the differences between type I and II HCs of the LES (Table
298 3).
299
300 Together these results are consistent with previous reports on key physiological
301 properties of type I and II HCs in amniote vestibular organs. The mature physiological
302 status of each HC type appeared to be preserved in LES HCs that failed to reverse their
303 orientation because GPR156 was inactivated.
304
305 **Hair cell physiology beyond the lateral extrastriolar domain: Variations in**
306 **properties were not related to loss of GPR156**
307
308 Loss of GPR156 does not impact HC orientation in the striola and MES, but *Gpr156* is
309 transcribed in all HCs across the maculae (Kindt et al., 2021). We thus investigated
310 transduction and adaptation in those zones as well (Fig. 4). While there was heterogeneity
311 across HCs, we saw no striking systematic differences with genotype in the voltage-gated
312 or mechanotransduction currents from control *vs. Gpr156* mutants (but note that the
313 statistical power of the comparisons is low, Table 4).
314
315 **Gpr156 impacted the mechanosensitive properties of lateral-line hair cells in**
316 **zebrafish**
317
318 Similar to otolith organs of mammals, each neuromast within the posterior lateral-line
319 system of zebrafish has two populations of HCs that enable the detection of anterior- or
320 posterior-directed fluid flow (Fig. 5A). To allow bi-directional detection, both Emx2 and
321 Gpr156 are required to reverse the orientation of one HC population so that it can detect
322 posterior flow (Fig. 5A) (Jiang et al., 2017; Kindt et al., 2021). Previous work has shown
323 that in wild-type animals, the mechanosensitive properties of HCs that detect anterior flow

324 (Emx2^{-}) are larger compared to those that detect posterior flow (Emx2^{+}) (Kindig et al.,
325 2023). Further, this work demonstrated that loss or gain of Emx2 in all lateral-line HCs
326 was able to not only alter HC orientation, but also increase and decrease
327 mechanosensitive responses respectively (Kindig et al., 2023). Our current results in the
328 mouse utricle did not detect significant differences in the mechanotransduction properties
329 of HCs lacking GPR156 (Fig. 2). Whether loss of Gpr156 alters the mechanosensitive
330 properties of lateral-line HCs is not known.
331
332 To address this question, we used a membrane-localized GCaMP6s reporter in HCs
333 (memGCaMP6s) (Kindt et al., 2021) to perform *in vivo* calcium imaging (Lukasz and Kindt,
334 2018) and. By imaging GCaMP6s signals in an apical plane containing the hair bundles,
335 we measured evoked, mechanosensation-dependent calcium signals during fluid-jet
336 stimulation. We used this approach to stimulate in both the anterior and posterior direction
337 and compared the magnitude of the mechanosensitive responses in lateral-line HCs in
338 both control (*gpr156*$^{+/-}$) and *gpr156* mutants. As shown previously, we could reliably
339 identify the orientation of control HCs (whether they sense posterior to anterior flow, P to
340 A) or the reverse, A to P) using this approach (e.g., Fig. 5B). We first verified that in control
341 animals, the magnitude of the mechanosensitive responses of HCs that detect anterior
342 flow was greater than those that detect posterior flow (e.g.: Fig. 5B and Fig. 5D, F).
343 Consistent with previous work, in *gpr156* mutants, we found that the majority of HCs only
344 responded to P to A flow (e.g., Fig. 5C) (Kindt et al., 2021). We next examined the
345 magnitude of the GCaMP6s response in these P to A HCs in *gpr156* mutants. If Gpr156
346 did not function downstream of Emx2 to alter the mechanosensitive properties of HCs,
347 we predicted that the response magnitude of these HCs would fall between that of P to A
348 and A to P control HCs. However, if Gpr156 does act downstream of Emx2, we predicted
349 that the response magnitude of the P to A HCs in *gpr156* mutants would resemble that of
350 P to A HCs in controls and be greater than that of A to P HCs in controls. Importantly, we
351 found that the magnitude of the mechanosensitive responses in *gpr156* mutants was
352 comparable to that of control P to A HCs (e.g., Fig. 5C and Fig. 5E-F). Further, the
353 mechanosensitive responses were significantly larger in *gpr156* mutants than control A
354 to P HCs (Fig. 5F).

355

356 Our analysis thus indicates that in *gpr156* mutants, lateral-line HCs show larger
357 mechanosensitive responses. These responses are similar to HCs in control animals that
358 respond to anterior flow (Emx2^{-}). Together, this data suggests that the EMX2-GPR156
359 mechanism driving HC orientation reversal also affects the mechanosensitive properties
360 of HCs in zebrafish neuromasts.

361

362 **Segregated afferent receptive fields were preserved in mouse utricles lacking**
363 **GPR156**

364

365 After characterizing the functional properties of HCs in mouse and zebrafish *Gpr156*
366 mutants, we examined whether GPR156 plays a role in orientation-selective afferent
367 innervation. Previous work has demonstrated that *Emx2* expression in the LES of the
368 mouse utricle and in HCs that sense posterior flow in the lateral line is required for
369 afferents to innervate HCs of similar (rather than opposing) orientation (Ji et al., 2022; Ji
370 et al., 2018). Whether GPR156 plays a similar role in direction-selective afferent
371 innervation is unknown.

372

373 To investigate whether afferent organization in the LES is disrupted by loss of GPR156,
374 we first compared the terminal fields of individual dye-filled calyx-bearing afferents in
375 *Gpr156*$^{del/+}$ *and Gpr156*$^{del/del}$ utricles. All LES calyces belong to dimorphic afferents, which
376 form both calyces on type I HCs and boutons on type II HCs. To examine terminal fields,
377 a fluorescent internal solution was injected into a calyx terminal within the LES during
378 whole-cell recordings. The fluorescent dye was then allowed to diffuse into the calyx and
379 from there throughout the terminal arbor.

380

381 Using this approach, we found that terminal arbors (receptive fields) in *Gpr156*$^{del/+}$ control
382 utricles (n = 12) comprised 1 or 2 calyces and as many as 65 boutons (median: 29) (Fig.
383 6A-C). The labeled afferent terminals were restricted to LES in all but one case (Fig. 6A).
384 In this single case, a terminal branch crossed the LPR, innervating 16 striolar HCs with
385 opposite orientation to the 12 LES HCs also innervated. In some filled LES afferents, a

386 thin branch originated below the epithelium (Fig. 6C, Supplemental video 1), as previously
387 described for chinchilla extrastriola (Fernandez et al., 1990). We also labeled a single
388 striolar calyx from a control utricle near the striolar/MES boundary; its terminal field was
389 excluded from the calbindin-negative MES (Fig. 6D).
390
391 When we performed dye labeling in *Gpr156*$^{del/del}$ utricles, the innervation patterns and the
392 size of terminal fields appeared similar to *Gpr156*$^{del/+}$ controls. In *Gpr156*$^{del/del}$ utricles, the
393 labeled LES afferents (n = 8) were also all dimorphic, terminating in up to three calyces
394 and 56 boutons (median: 23). The labeled receptive fields did not cross the striola/LES
395 border (Fig. 6E-G). We also did not observe fiber branches extending across the border
396 from parent axons (Fig. 6E-G; Supplemental video 2). As observed in the lone *Gpr156*$^{del/+}$
397 striolar afferent (Fig. 6D), *Gpr156*$^{del/del}$ afferents with the main dendritic fiber terminating
398 in the striola (n = 4) contacted relatively few HCs, and receptive fields were restricted to
399 the calbindin-positive region (Figure 6H).
400
401 To confirm and complement dye-filling results at the whole organ level, we used a new
402 genetic approach to specifically label afferents innervating EMX2^{+} HCs in the LES.
403 Interestingly, when breeding the *Advillin-Cre* strain (Zhou et al., 2010) with the *Tigre Ai140*
404 reporter (Daigle et al., 2018), we only observed Cre recombination and EGFP expression
405 in vestibular ganglion neurons that contacted HCs in the lateral utricle region (Fig. 7A).
406 Close examination revealed clear labeling of HC calyces in the LES, and occasionally in
407 OCM^{+} HCs in the lateral striola (Fig. 7B, arrowheads). We confirmed that similar to OCM^{-}
408 EGFP^{+} HCs in the LES, these OCM^{+} EGFP^{+} HCs were invariably oriented towards the
409 medial edge (Fig. 7C). This demonstrated that *Advillin* expression defines a population of
410 neurons whose peripheral processes closely segregate with HC orientation, irrespective
411 of striolar (OCM^{+}) or extrastriolar (OCM^{-}) HC identity. Importantly, HC innervation by
412 *Advillin*-positive neurons was unchanged in *Gpr156*$^{del/del}$ mutants (Fig. 7A-B). We
413 observed equivalent numbers of OCM^{+} HCs innervated in the lateral striola in *Gpr156*$^{del/del}$
414 mutants compared to controls (Mann-Whitney p=0.74; average OCM^{+}/EGFP^{+} HCs per
415 utricle: *Gpr156*$^{del/+}$: 20.25, *Gpr156*$^{del/del}$:19.25; 3 animals and 4 utricles per genotype; no
416 OCM^{+}/EGFP^{+} HCs oriented towards the lateral edge were recorded in either genotype).

In summary, we detected no anomaly in afferent receptive fields in utricles lacking GPR156 and thus lacking a LPR, showing that the tendency of afferents to innervate HCs on one side of the LPR is not controlled by GPR156 or HC orientation.

Afferent firing patterns were preserved in mouse utricles lacking GPR156

Our innervation data suggested that HCs in zones demarcated by the LPR are still innervated by distinct populations of afferent neurons in *Gpr156*$^{del/del}$ mutants. We next investigated whether the LES afferent population retains normal physiology. Striolar afferents have highly irregular inter-spike intervals, while extrastriolar afferents in both LES and MES have much more regular inter-spike intervals (Goldberg, 1991; Goldberg, 2000; Goldberg et al., 1990). Associated with the difference in spike timing regularity are zonal differences in response dynamics and information encoding capacity (e.g., (Jamali et al., 2019)). The spike timing difference is considered to reflect differences in afferents' excitability as conferred by their intrinsic ion channels, with regular afferents being more excitable (Kalluri et al., 2010; Ventura and Kalluri, 2019). To test for effects of *Gpr156* inactivation on afferent excitability, we injected small depolarizing current steps into LES calyces through the whole-cell recording pipette and measured current threshold for spiking, I_{thresh}, and the numbers of spikes evoked by each current step.

As reported (Gonzalez-Garrido et al., 2021; Ono et al., 2020), I_{thresh} evoked 1-to-several spikes but increments beyond I_{thresh} evoked more sustained firing (Fig. 8A-B). No difference was observed across genotypes (Table 5): in both *Gpr156*$^{del/+}$ afferents (n = 18) and *Gpr156*$^{del/del}$ afferents (n = 20), mean I_{thresh} was ~100 pA and ~95% of afferents produced sustained spiking at $3\times I_{thresh.}$ These results suggest that afferent firing patterns, and likely the underlying ion channel expression, are unaltered in the LES of *Gpr156*$^{del/del}$ utricles, despite abnormal HC orientation.

Gpr156 was not required for afferent selectivity or synaptic pairing in zebrafish lateral-line

448

449 We next expanded our analysis to determine whether loss of Gpr156 impacts afferent
450 selectivity in the lateral-line. For this analysis we used mosaic expression of
451 *neuroD:tdTomato* to label single lateral-line afferent neurons. After identifying *gpr156*
452 mutant and control *(gpr156*$^{+/-}$) animals with labeled fibers, we immunolabeled to visualize
453 orientation (phalloidin), HC bodies (MYO7), and cell type (presence or absence of Emx2).
454 We then used confocal microscopy to image the innervation pattern of single afferents.
455

456 Consistent with previous results, some afferent fibers selectively contacted Emx2^{-} HCs
457 with hair bundles oriented to respond to anterior flow in control animals (Fig. 9A-H). Other
458 afferent fibers selectively contacted Emx2^{+} HCs with hair bundles oriented to respond to
459 posterior flow (Supplemental fig. 1A-H). We then examined the innervation patterns of
460 afferent fibers in *gpr156* mutants. Similar to controls we were able to identify fibers with a
461 clear preference for Emx2^{-} or Emx2^{+} HCs (Fig. 9I-P, Supplemental fig. 1I-P). Importantly,
462 in *gpr156* mutants, afferent fibers innervated HCs based on the presence or absence of
463 Emx2, despite all HCs responding to anterior flow.
464

465 Following this initial assessment, we quantified the percentage of HCs per neuromast that
466 were innervated by each afferent fiber. We found that *gpr156* mutant fibers innervated a
467 similar percentage of HCs per neuromast compared to controls (Fig. 9Q, control: 38.90 %
468 ± 2.40, n = 18, *gpr156* ko: 41.31 % ± 2.33, n = 23, p = 0.48). We also quantified how
469 selective each afferent fiber was for Emx2^{+} or Emx2^{-} HC. For each afferent fiber, we
470 calculated the percentage of either Emx2^{+} or Emx2^{-} HCs innervated out of the total
471 number of innervated HCs. In both control and *gpr156* mutants, afferent fibers showed a
472 high selectivity (Fig. 9R, control: 85.06 % ± 4.32, n = 18, *gpr156* ko: 81.29 % ± 3.17, n =
473 23, p = 0.48). We split this dataset and examined the selectivity of afferent fibers that
474 preferentially contacted either Emx2^{-} or Emx2^{+} HCs (Fig. 9S-T). This analysis revealed
475 that in control and *gpr156* mutants, both afferent fiber types were highly selective
476 (afferents contacting Emx2^{-} cells, control: 81.41 % ± 7.90, n = 8, *gpr156* ko: 79.37 % ±
477 4.73, n = 10, p = 0.82; afferents contacting Emx2^{+} cells, control: 87.99 % ± 4.75, n = 10,
478 *gpr156* ko: 82.80 % ± 4.38, n = 13, p = 0.43). Overall, our single fiber labeling revealed

479 that Gpr156 is not required for afferent fibers to selectively innervate HCs based on the
480 presence or absence of Emx2.
481
482 To extend this analysis, we examined synaptic pairing in *gpr156* mutants. Previous
483 research found that along with inappropriate innervation, there is an increase in the
484 amount of unpaired pre- and post-synapses in *emx2* mutants (Ji et al., 2018). We
485 immunostained control along with *gpr156* and *emx2* mutant HCs with Ribeye b to label
486 presynapses and pan-MAGUK to label postsynapses (Fig. 10A-C). We then quantified
487 the number of complete immunolabeled synapses per HC. Among all genotypes, the
488 number of complete synapses was unaltered (Fig. 10D, control 3.56 ± 0.06, n = 9
489 neuromasts, *gpr156* ko: 3.61 ± 0.10, n = 16 neuromasts, p = 0.74; control 3.51 ± 0.27, n
490 = 9 neuromasts, *emx2* ko: 3.67± 0.08 n = 9 neuromasts, p = 0.50). We also quantified
491 unpaired pre- and post-synapses. Similar to previous results, there were more unpaired
492 pre- and post-synapses per neuromast in *emx2* mutants compared to controls (Fig. 9E-
493 F, presynapses, *emx2*$^{+/+}$ or *emx2*$^{+/-}$ control 2.00 ± 0.53, n = 9 neuromasts, *emx2* ko: 4.22
494 ± 0.70, n = 9 neuromasts, p = 0.02; postsynapses, control 1.44 ± 0.56, n = 9 neuromasts,
495 *emx2* ko: 6.56 ± 0.78, n = 9 neuromasts, p < 0.0001). In contrast, in *gpr156* mutants,
496 there was no increase in unpaired pre- or post-synapses per neuromast compared to
497 controls (Fig. 10E-F, presynapses, *gpr156*$^{+/-}$ control 2.11 ± 0.31, n = 9 neuromasts,
498 *gpr156* ko: 1.68 ± 0.23, n = 16 neuromasts, p = 0.29; postsynapses, control 0.33 ± 0.17,
499 n = 9 neuromasts, *gpr156* ko: 0.75 ± 0.17, n = 16 neuromasts, p = 0.12). A lack of unpaired
500 pre- and post-synapses in *gpr156* mutants further confirms that Emx2 but not Gpr156
501 impacts afferent innervation in lateral-line HCs.
502
503 In summary, *Gpr156* inactivation does not appear to impact afferent selectivity in either
504 mouse or zebrafish. This is in sharp contrast with results in *Emx2* mutants, where
505 orientation-specific HC afferent innervation is profoundly altered in mouse and zebrafish
506 (Ji et al., 2022; Ji et al., 2018). It follows that HC orientation per se does not dictate afferent
507 selectivity, with EMX2 likely using a different effector(s) than GPR156 in this context. Thus,
508 afferent studies confirm that the *Gpr156*^{del} model is well-suited to investigate specifically
509 how the reversal of HC orientation in otolith and lateral line organs serves organ function.

510

511 ***Gpr156* mutant mice had defects in otolith-driven, but not canal-driven, vestibular**
512 **behaviors**

513

514 In mammals, only otolith organs (utricle, saccule) have a LPR. Therefore, the absence of
515 a LPR in *Gpr156* mutants should only affect otolith-driven reflexes and behaviors. In order
516 to test this prediction we compared *Gpr156* control and mutant mice on a number of tests
517 that can discriminate between otolith and canal inputs.

518

519 <u>Normal posture, balance beam but impaired swimming performance in *Gpr156* mutants</u>
520 To assess how loss of the LPR affects vestibular functions, we first determined whether
521 *Gpr156* mutant mice showed postural/balance impairments. Visual and quantitative
522 assessments did not reveal circling or head tremor behaviors in $Gpr156^{del/del}$ mice at rest
523 (Supplemental fig. 2). Additionally, we conducted basic standard behavioral tests that
524 involve subjective scoring: (1) tail hanging, (2) air righting, and (3) contact inhibition of
525 righting. Both control and $Gpr156^{del/del}$ mice scored 0 (where 0=normal, see Methods) on
526 each of these behavioral tests (Supplemental fig. 3A-C).

527

528 After this initial assessment, we next subjected mice to more challenging balance tests
529 including walking along a narrow balance beam and swimming. On the balance beam,
530 both $Gpr156^{del/del}$ and $Gpr156^{del/+}$ mice showed normal coordination (Fig. 11A). However,
531 when $Gpr156^{del/del}$ mice were placed in water, they demonstrated severely impaired
532 swimming compared to $Gpr156^{del/+}$ controls. This impairment was characterized by
533 underwater tumbling and the inability to maintain normal upright posture in the water. All
534 mice were rescued within 60 seconds and the average time of rescue was significantly
535 lower in $Gpr156^{del/del}$ compared to control mice (Fig. 11B; $Gpr156^{del/+}$ controls= 49.9±3.0s;
536 $Gpr156^{-del/del}$= 17.4±2.7s; P<0.0001). Overall, these results indicated that GPR156 is
537 required for vestibular function important for swimming behavior.

538

539 We hypothesized that markedly impaired swimming performance could be due to deficits
540 in the otolith rather than semicircular canal dependent pathways. To test this proposal,

541 we quantified eye movements generated by two different vestibulo-ocular reflex
542 behaviors, one driven by activation of the semicircular canals (angular vestibular-ocular
543 reflex, or angular VOR) and the other driven by activation of the otoliths (off-axis vertical
544 rotation, or OVAR).
545
546 Normal aVOR and OKR responses in *Gpr156* mutants
547 We first quantified the angular vestibulo-ocular reflex in *Gpr156*$^{del/del}$ and *Gpr156*$^{del/+}$
548 control mice in darkness (VORd). The angular VOR was evoked by rotating the animal
549 sinusoidally around earth vertical axis. To quantify the angular VORd we computed the
550 gain and phase for each testing frequency (0.2, 0.4, 0.8, 1, and 2Hz, ±16°/s). During
551 VORd, both control and *Gpr156*$^{del/del}$ mice displayed robust compensatory eye
552 movements, which increased as a function of frequency (Fig. 12A-B). Further, to confirm
553 that there was no visual deficit in *Gpr156*$^{del/del}$ mice, we also tested their optokinetic reflex
554 (OKR) by rotating a patterned visual surround sinusoidally about earth vertical axis at
555 the same testing frequencies, while the animal remained stationary (see Methods). The
556 OKR responses of *Gpr156*$^{del/del}$ and control mice were comparable, confirming that there
557 was no visual deficit in *Gpr156* mutants (Fig. 12C-D). For the sake of completeness, we
558 quantified the angular VOR evoked in the light (VORl) by rotating the animal sinusoidally
559 around earth vertical axis, while the patterned visual surround remained stationary.
560 Again, we found no difference in the VORl response of *Gpr156*$^{del/del}$ versus control mice
561 in this lit environment (Figure 12E-F). Finally, we tested whether *Gpr156*$^{del/del}$ mice
562 demonstrated normal ability to adapt their angular VOR. We used a standard angular
563 VOR motor learning protocol (see Methods) in which we carried out 30-minute-long VOR
564 gain-down training for both control and *Gpr156*$^{del/del}$ mice. Head restrained mice were
565 rotated with the visual surround in phase. The training stimulus was 2 Hz with a peak
566 velocity of 16°/s. The learning efficacy was assessed by quantifying change in the VOR
567 gain after training. In both control and *Gpr156*$^{del/del}$ mice, this VOR motor learning
568 protocol produced a significant reduction in VOR gain after training (Supplemental fig.
569 4A-B). Overall, *Gpr156*$^{del/del}$ and control mice demonstrated a comparable percent
570 change of gain decrease at each testing frequencies (Supplemental fig. 4C). Together,
571 our VOR and OKR results indicated normal semicircular canals-driven responses in

572 *Gpr156*$^{del/del}$ mice.

573

574 Altered OVAR responses in *Gpr156* mutants

575 As no defects were apparent in semicircular canal-mediated behavior, we next tested
576 whether otolith-mediated vestibulo-ocular reflex behaviors were impaired in *Gpr156*$^{del/del}$
577 mice. For this assessment, we recorded eye movements while the mouse was tilted 17°
578 off-the vertical axis (i.e., off-vertical axis rotation (OVAR)), and then rotated at a constant
579 velocity (50°/s for 72 sec). The eye velocity evoked by this paradigm comprised two
580 different responses: (1) a transient canal-mediated response that decayed over the first
581 10-15 sec and (2) an otolith-mediated steady-state response in which eye velocity
582 oscillated around a constant bias with a sinusoidal waveform (Figure 12G). Overall, our
583 analysis revealed that transient OVAR responses did not differ between control and
584 *Gpr156*$^{del/del}$ mice, supporting the proposal that absence of GPR156 did not affect canal-
585 related ocular responses. In contrast, steady-state OVAR responses demonstrated a
586 significantly impaired bias in *Gpr156*$^{del/del}$ mice as compared to controls (Figure 12G-H).
587 The OVAR of *Gpr156*$^{del/del}$ mice was characterized by a significantly reduced bias relative
588 to controls (*Gpr156*$^{del/del}$: bias=0.039 ± 0.26 versus control: bias=3.85 ± 0.54, P = 4.03E-
589 5). Thus taken together, these results show that the absence of HC reversal in
590 *Gpr156*$^{del/del}$ alters otolith-mediated OVAR responses. This in turn may explain the
591 swimming deficits observed (Fig. 11B).

592

593

594

595 **DISCUSSION**

596

597 **Hair bundle orientation vs. zonal identity**

598 Taken together, our observations in utricles lacking GPR156 agree with other evidence
599 that in mouse vestibular epithelia, HC orientation is controlled separately from other
600 zonally differentiated properties of either HCs or afferents. Prior evidence includes data
601 from *Emx2* knockouts also exhibiting loss of the LPR without altering zoning (Jiang et al.,
602 2017) and data showing that inactivating cytochrome P450 family 26 deletes striolar
603 identity without affecting HC orientation (Ono et al., 2020). This conclusion stands in
604 contrast to zebrafish lateral line results, where transduction properties vary with HC
605 orientation depending on Emx2 (Kindig et al., 2023) and Gpr156 (this study).

606

607 **Asymmetrical mechano-electrical transduction**

608 Zebrafish lateral-line HCs use a combination of 2 mechanosensitive channels, Tmc2a
609 and Tmc2b (Chou et al., 2017). In the posterior lateral line, Emx2^{+} HCs that sense
610 posterior flow rely on primarily on Tmc2b, while Emx2^{-} HCs that sense anterior flow rely
611 on both Tmc2a and Tmc2b. Recently, a functional asymmetry was discovered between
612 anterior- and posterior-sensitive HCs: Emx2^{+} HCs that rely primarily on Tmc2b have
613 smaller mechanosensitive responses compared to Emx2^{-} HCs that rely on both Tmc2a
614 and Tmc2b. (Kindig et al., 2023). This work raises the possibility that the transcription
615 factor Emx2 inhibits *tmc2a* transcription to reduce mechanosensitive responses in HCs
616 sensing posterior flow. In our present study we find that functional asymmetry was also
617 lost in *gpr156* mutants (Fig. 5). In the context of mouse HC orientation, EMX2 is necessary
618 and sufficient to enrich and polarize GPR156 at HC apical junctions and reverse HC
619 orientation (Kindt et al., 2021). As the Gpr156 receptor is unlikely to act transcriptionally,
620 zebrafish Emx2 may act through Gpr156 to impact Tmc2a/2b function. For example,
621 polarization of Gpr156 at apical junctions may limit scaffolding or transport of Tmc
622 proteins to homomeric channels composed of Tmc2b. Overall, our work in zebrafish
623 indicates that both Emx2 and Gpr156 are important to dictate HC orientation and the
624 mechanosensitive properties of HCs with opposing orientations.

625

626 We did not see a clear impact of GPR156 loss on the transduction properties of *Emx2*$^{+}$
627 HCs in the mouse utricle (Fig. 2-4). Subtle effects remain possible, however, given the
628 variance in single-cell electrophysiological data from both control and mutant mice.
629 Nevertheless, current results are consistent with normal HC function in the *Gpr156* mouse
630 mutant, a prerequisite to interrogate how non-reversed HCs affects vestibular behavior.
631

632 **Importance of the LPR for vestibular function**

633 The brain combines information from the maculae and cristae with inputs from other
634 modalities, including the somatosensory and visual systems, to compute a representation
635 of our self-motion and spatial orientation (reviewed in (Cullen, 2019). Our present findings
636 demonstrate that GPR156 is *not* required for macular HCs to selectively contact different
637 afferents across the LPR. Accordingly, we predicted that HCs that fail to reverse in the
638 lateral utricle of *Gpr156* mutants would lead to deficits in paradigms that test macular
639 contributions to behavioral responses. Indeed, *Gpr156* mutant mice demonstrated
640 impaired performance on two tests that engage the otolith organs: swimming and off-
641 vertical-axis rotation (OVAR). First, during swimming, impaired spatial orientation results
642 from the combined altered otolith input and reduced somatosensory feedback due to the
643 aqueous environment. Second, *Gpr156* mutant mice displayed impaired sustained
644 responses to off-vertical axis rotation (OVAR). While initial eye movement response to
645 OVAR is mediated by stimulation of semicircular canal HCs, the canal response decays
646 such that sustained eye movement is solely driven by the otolith stimulation (Beraneck et
647 al., 2012; Ono et al., 2020). Quantification of the sustained responses revealed a marked
648 reduction in this otolith-mediated reflex response. Confirming that these deficits are
649 specific to otolith function, the *Gpr156* mutant mice did not show overt vestibular
650 dysfunction such as spinning or head tilt that can arise with global dysfunction of
651 vestibular epithelia. Further, they displayed normal performance during testing that
652 selectively engaged superior canal organs, namely angular VOR in the light and dark.
653 This latter finding was predicted; because HC orientation is unchanged in *Gpr156* mutant
654 cristae, the coding properties of semicircular canal afferents should be unchanged and
655 would therefore produce a normal angular VOR upon specific stimulation of canal
656 ampullae.

657

658 **Comparing vestibular phenotypes of *Gpr156* and *Emx2* mutants**

659 *Gpr156* does not appear to be significantly expressed in the central nervous system
660 according to the Allen Brain Atlas (Lein et al., 2007). In addition, *Advillin-Cre* tracing and
661 dye-filling experiments (Fig. 6-7) showed that vestibular ganglion neurons still selectively
662 innervated LES HCs even when lacking GPR156. We thus speculate that HC signals in
663 the LES zone of *Gpr156* mutants are relayed to the cerebellum (Ji et al., 2022; Maklad et
664 al., 2010) via the central projection of *Advillin*$^{+}$ neurons as usual, but with abnormal (non-
665 reversed) response polarity. Overall, it appears unlikely that vestibular deficits observed
666 in our constitutive *Gpr156* mouse mutants reflect defective neuronal activity in addition to
667 a missing LPR. That said, we cannot entirely rule out another role of GPR156 beside its
668 regulation of HC orientation. This could be addressed in a follow-up study by limiting
669 *Gpr156* inactivation to HCs.

670

671 It is interesting to compare vestibular-related behaviors between the *Gpr156* and *Emx2*
672 mouse models in light of established similarities and differences in protein distribution and
673 function (Ji et al., 2022; Jiang et al., 2017; Kindt et al., 2021). Regarding behavior, this
674 study and work by Ji et al., 2022 agree that vestibular deficits in each model are relatively
675 mild (normal balance beam, VOR and OKR). *Emx2* inactivation in HCs (*Gfi1-Cre*) showed
676 impaired swimming ability, but defects were less severe and different in nature compared
677 to constitutive *Gpr156* mutants. *Gpr156* mutants displayed substantial difficulty in
678 maintaining their orientation in water, and frequently rolled over such that they needed to
679 be rescued. In contrast, *Emx2* mutants did not need rescue and were described as
680 demonstrating “frantic” swimming behavior, spending more time trying to climb out of the
681 water as compared to their littermate controls. OVAR highlighted otolith-specific defects
682 in *Gpr156* mutants but was not performed in *Emx2* mutants.

683

684 GPR156 acts downstream of EMX2 to regulate hair bundle orientation, and perhaps
685 mechanosensitivity in zebrafish. Another significant new result in the current study is to
686 show that afferent projections segregate with HC orientation and not with zonal identity
687 (Fig. 7; Advillin neuron labeling), yet segregation does not depend on HC orientation since

688 it is unchanged in mouse and zebrafish *Gpr156* mutants (Fig. 6-10). It follows that EMX2
689 must influence afferent segregation (Ji et al., 2022; Ji et al., 2018) via other effectors
690 unrelated to HC orientation. Accordingly, Ji and colleagues concluded that EMX2
691 regulates HC orientation and afferent patterning independently, with *Emx2* expression in
692 support cells critical for proper afferent contacts with HCs (Ji et al., 2022). This aligns well
693 with previous evidence that *Gpr156* is only expressed in HCs (Kindt et al., 2021).
694
695 Ji and colleagues also used specific inactivation of the transduction protein TMIE in the
696 LES (*Emx2-Cre*) to silence the *Emx2*$^{+}$ HC population. Interestingly, as with *Emx2* mutants,
697 they did not observe severe behavioral defects, and swimming ability in particular was
698 not obviously compromised in contrast to *Gpr156* mutants. It should be noted however
699 that while the *Gpr156 KO* and *Emx2-Cre; Tmie cKO* models both lack a normal
700 complement of bidirectional responses, they provide different forms of aberrant linear
701 acceleration signals. In the *Tmie* cKO model, LES HC inputs to the cerebellum are
702 missing but in the *Gpr156* model they are retained and of opposite nature since LES HCs
703 fail to reverse their orientation.
704
705 Several considerations could potentially explain why the *Gpr156* model appears to display
706 more severe behavioral defects compared to the *Emx2* models. First, HC or afferent
707 properties were not tested in *Emx2* mutants (Ji et al., 2022) and may be defective. Second,
708 compounded HC orientation and afferent defects in the *Emx2* mutants could dampen the
709 deleterious consequence of having LES HCs drive a neuronal response of reversed
710 polarity. Afferent defects in *Emx2* mutants were reported during embryogenesis (E16.5)
711 and innervation could further degenerate in adults, further dampening the consequence
712 of non-reversed HC activity in the LES. It is worth noting that aberrant vestibular afferent
713 signals are clinically more deleterious than absent signals, which perhaps explains why
714 properly relayed yet aberrant signals from LES HCs in *Gpr156* mutants result in
715 behavioral defects worse than observed in *Emx2* or *Emx2-Cre; Tmie cKO* models.
716
717 In conclusion, the *Gpr156* mutant mouse model is well-suited to specifically interrogate
718 how HC orientation reversal and the resulting LPR influence vestibular function because

it appears to lack confounding afferent patterning defects. In future studies, this model could be improved by limiting *Gpr156* inactivation to HCs.

ACKNOWLEDGMENTS

This work was supported by the National Institute on Deafness and Other Communication Disorders (NIDCD) grant R01DC018304 (to RAE, KEC and BT), R01DC015242 (to BT) and NIDCD Intramural Research Program Grant 1ZIADC000085-01 (to KK).

AUTHOR CONTRIBUTION

BT, RAE, KEC and KK conceived the study and supervised the work. KO, KK, AJa, NCH, AJu and HHVC designed, performed and analyzed experiments. MRD shared the information that *Advillin-Cre* labels afferent neurons innervating *Emx2*$^{+}$ macular regions. BT, RAE, KEC and KK wrote the manuscript and secured funding.

COMPETING INTERESTS

The authors declare no competing interest.

DATA AVAILABILITY

Source data will be deposited in publicly accessible repositories by each contributing laboratory.

747 **METHODS**

748

749 **Mouse strains and husbandry**

750 The *Gpr156*^{del} strain (*B6N(Cg)-Gpr156tm1.1(KOMP)Vlcg/J*; MGI:5608696) was produced
751 by the Knockout Mouse Project (KOMP) and studied previously in (Kindt et al., 2021).
752 The *Advillin-Cre* strain is *B6.129P2-Avil*$^{tm2(cre)Fawa/J}$ (MGI: 6196038) (Zhou et al., 2010).
753 The *Tigre Ai140* strain is *B6.Cg-Igs7*$^{tm140.1(tetO\text{-}EGFP,CAG\text{-}tTA2)Hze}$ (MGI: 5904001) (Daigle et
754 al., 2018). Some whole-cell patch clamp recordings were obtained from CD1 mice
755 (Charles River Laboratories USA). All animals were maintained in standard housing and
756 all animal work was reviewed for compliance and approved by the Animal Care and Use
757 Committees of The Jackson Laboratory (anatomical experiments), the University of
758 Chicago (cellular electrophysiology and afferent labeling experiments), and the Johns
759 Hopkins University School of Medicine (behavioral experiments).

760

761 **Mouse immunofluorescence and imaging (Figure 1, Figure 7)**

762 Temporal bones of adult animals were isolated, oval windows were cleared and the
763 cochlear apex was punctured to allow better access to the fixative. Samples were then
764 fixed in paraformaldehyde (PFA 4%) overnight at 4°C, rinsed in PBS and incubated
765 overnight in 4% Ethylenediaminetetraacetic acid (EDTA) at room temperature for
766 decalcification. Both the trio (utricle and crista) and the saccule were dissected from the
767 bone and their epithelium exposed. After dissection, samples were permeabilized and
768 blocked in PBS with 0.5% Triton-X100 and bovine serum albumin (1%) for at least at 1
769 hour at room temperature. For SPP1/Osteonpontin staining, temporal bones were
770 immediately dissected to isolate the trio and the saccule and expose their epithelium, and
771 an eyelash was used to scrape off the otoconia, Samples were then fixed in PFA 4% for
772 1h at room temperature before being permeabilized and blocked as described previously.
773 Primary and secondary antibodies were each incubated overnight at 4°C in PBS, and
774 fluorescent dye-conjugated phalloidin was added to secondary antibodies. Samples were
775 washed 3 times in PBS + 0.05% Triton-X100 after each antibody incubation before being
776 finally post fixed in PFA 4% for at least 1 hour at room temperature. Primary antibodies
777 used were:

778 Mouse anti-MYO7A (Developmental Studies Hybridoma Bank/DSHB 138-1, 1:1000)
779 Goat anti-OCM (Invitrogen, PA547832, 1:200)
780 Goat anti-SPP1 (R&D Systems, AF808, 1:200)
781 Rabbit anti-PCNT (Biolegend, PRB432C, 1:400)
782 Goat anti-SOX2 (R&D Systems, AF2018, 1:200)
783 Secondary antibodies used were raised in donkey and coupled with AlexaFluor (AF) 488,
784 555, or 647 (donkey anti-rabbit 488 (A-21206), donkey anti-mouse 647 (A-31571), donkey
785 anti-goat 555 (A-21432); Thermofisher Scientific). Fluorescent conjugated phalloidin was
786 used to reveal F-actin (CF405 (89138-126); Biotum).
787 Confocal images were captured on a line scanning confocal microscope (LSM8000) using
788 Zen 2.6 software, the Airyscan detector in confocal mode, and either a 20× or a 63× 1.4
789 NA oil objective lens (Carl Zeiss AG). Images show a single optical plane unless stated
790 otherwise in the figure legend.
791
792 **Mouse immunostain quantification (Figure 1, Figure 7)**
793 All images were processed using Adobe Photoshop (CC2020), and the same image
794 treatment was applied across genotypes for each experiment. All quantifications included
795 at least three animals of each genotypes, and all values plotted in the study, as well as
796 animal cohort size (N), HC number and stereocilia number (n) are detailed in legends. To
797 quantify striolar surface, striolar density, as well as HC Type I and II density by region,
798 images were captured using a DM5500B fluorescence microscope using the Leica
799 Application Suite (LASX) and a 20x objective (Leica). Striolar surface was measured
800 using the polygon selection and area tools in Fiji/ImageJ to define the striola based on
801 the Oncomodulin staining. Striolar density was measured by using the cell counter tool in
802 Fiji/ImageJ to obtain the total number of Oconmodulin positive HCs. That number was
803 then normalized by the total striolar surface previously measured to obtain a final number
804 of HCs per 1000μm^2. To measure Type I and Type II HC density by region, three regions
805 of interest (ROI) were defined centrally of either 130x50μm (utricle) or 150x40μm
806 (saccule). The lateral extrastriolar (LES) domain was placed 20μm inside the macula
807 starting from the lateral edge of the utricle, encompassing most of the region lateral to the
808 line of polarity reversal (LPR). The striolar domain was defined immediately adjacent to

809 the LES domain based on the LPR and oncomodulin signal in controls. The medial
810 extrastriolar (MES) domain started 50µm medial to the striolar domain. The anterior
811 extrastriolar domain (ANT) was placed 10µm from the anterior edge of the saccule. The
812 striolar domain was defined 20µm posterior to the ANT domain based on oncomodulin
813 staining in controls, and the posterior extrastriolar domain (POST) was defined 50µm
814 posterior to the striolar domain. The location of these domains is illustrated in Fig.1A. The
815 same fields and spacing were next used for the *Gpr156*$^{del/del}$ mutants. The cell counter
816 plugin in Fiji/ImageJ was used to count HCs in each ROI.
817
818 **Data analysis and statistics – mouse anatomy (Figure 1, Figure 7)**
819 All data were plotted in Prism 9 (GraphPad). Striolar surface, HC density and number of
820 Type I and type II HC density in each region of the maculae were plotted individually.
821 Their distribution was framed by 25-75% whisker boxes where exterior lines show the
822 minimum and the maximum, the middle line represents the median, and + represents the
823 mean. Difference of data distribution was tested using Mann-Whitney U (non-parametric,
824 unpaired t-test) for striolar surface and HC density, and 2-way ANOVA with Sidak's
825 multiple comparison for type I and type II HCs.
826
827 **Mouse hair cell and afferent electrophysiology (Figures 2-4, Figure 8)**
828 We followed procedures described in (Gonzalez-Garrido et al., 2021) to prepare and
829 record from HCs and calyceal afferent terminals in semi-intact utricles comprising the
830 sensory epithelium and attached distal vestibular nerve including the vestibular ganglion.
831 Recordings were analyzed for 83 cells from 57 *Gpr156* heterozygotes and 93 cells from
832 73 *Gpr156*-null animals.
833
834 Preparation. Following protocols approved by the University of Chicago Animal Care and
835 Use Committee, mice were deeply anesthetized with gaseous isoflurane and then
836 decapitated to allow dissection of the utricles and attached nerve and ganglion. The
837 preparations were dissected in our *standard bath (external) solution*: cold Leibovitz's-L15
838 medium (L15, Gibco, #41300-021) supplemented with 10 mM HEPES (4-(2-
839 hydroxyethyl)-1-piperazineethanesulfonic acid) (~315 mmol/kg, pH 7.4). The utricles

840 were then treated with L15 containing proteinase XXIV (100 mg/ml, Sigma, St. Louis, MO
841 #P8038) for 11 min at room temperature to facilitate mechanical removal of the otolithic
842 membrane. The epithelium was mounted on a cover slip with glued glass fibers and
843 placed in a recording chamber on a microscope (Zeiss, Axio Examiner A1) equipped with
844 Nomarski and fluorescence optics.
845
846 Recording. For whole-cell recording, pipettes (R6, King Precision Glass) were heat-pulled
847 (PC100, Narishige) and parafilm-wrapped to reduce capacitance. Pipette resistances
848 were 4-5 MΩ for the standard internal and external solutions. Standard internal solution
849 contained (in mM): 135 KCl, 0.1 $CaCl_2$, 3.5 $MgCl_2$, 3 Na_2ATP, 5 creatine phosphate (Na
850 salt), 0.1 Na-cAMP, 0.1 Li-GTP, 5 EGTA, and 10 HEPES, plus ~28 mM KOH to bring pH
851 to 7.3 and osmolality to ~300 mmol/kg. Internal solution was supplemented with
852 sulforhodamine 101 (1 mg/100 ml; Thermo Fisher Scientific) for visualization of recorded
853 hair cells. The bath (external solution) was modified L15 (described above), which was
854 perfused during the experiment.
855
856 We were able to locate LES, striola or MES despite loss of the LPR because anatomical
857 features of the striola are maintained in the otolith organs of *Gpr156* $^{del/del}$ mice (Kindt et
858 al., 2021), and some of these (hair bundle size, spacing of HCs, abundance of complex
859 calyces) are visible in live tissue with Nomarski optics. Usually we aimed for HCs or
860 calyces >50 μm away from zonal boundaries to avoid confusion over zone. In one
861 experimental series, however, we focused on the zonal boundary to see whether afferents
862 respected zonal boundaries in Gpr156-deleted mice.
863
864 To record in whole-cell mode from a specific HC or afferent calyx, we cleaned the cell
865 membrane by the outflow of pipette solution and applied gentle suction to promote giga-
866 seal formation and membrane rupture. Stimulus protocols and data acquisition were
867 implemented by the patch clamp amplifier (model EPC-10, HEKA Elektronik) controlled
868 by Patchmaster software. Data were digitized at sampling intervals of 10 or 20
869 microseconds. Pipette and membrane capacitive currents were nulled and series
870 resistance (R_s) was compensated by 80% on-line with the amplifier's controls. Voltages

871 were corrected offline for the liquid junction potential (–4 mV) and the voltage error due
872 to residual R_s (20% of total R_s, 8.1 ± 0.1, n = 207).
873
874 Mechanical stimulation of mouse hair cells. Hair bundles were deflected with a rigid probe
875 (pulled glass pipette, BF120-60-10, Sutter instrument Company) glued to a piezoelectric
876 bimorph ceramic and brought into contact with the staircase of stereocilia ('back' of the
877 bundle) at ~half-height. Displacement of the probe to driving voltage was calibrated with
878 a CCD camera, yielding a scale factor 330-410 nm/V, depending on the probe. Probe
879 motion recorded with a photodiode (PIN-6D, United Detector Technology) revealed a
880 primary resonance at 1900-2000 Hz. To attenuate this ringing, the voltage input to the
881 bimorph was low-pass filtered (8-pole Bessel filter, Model 900, Frequency Devices) set
882 at 1 kHz, for a step rise time (10-90%) of ~300 μs.
883
884 Mechanotransduction current was recorded in voltage-clamp mode with the holding
885 potential (HP) of –94 mV and –84 mV for type I and type II HCs, respectively. The larger
886 negative potential for type I HCs was chosen to reduce $g_{K,L}$ and so improve the voltage
887 clamp. Responses to three identical displacement step protocols were averaged and low-
888 pass filtered off line (corner frequency, 2 kHz, 8-pole Bessel filter, as above). Step
889 protocols comprised either 20 or 40 displacement steps iterated by 100 nm or 35 nm,
890 respectively, and beginning slightly negative to the resting bundle position. Transduction
891 sensitivity and adaptation was analyzed in 49 HCs with I_{max} > 150 pA (23 HCs from
892 heterozygotes and 26 HCs from null mutants), as described next.
893
894 **Quantification of mouse electrophysiological data**. Analysis of I_{MET} properties is
895 described elsewhere (Songer and Eatock, 2013; Vollrath and Eatock, 2003). Briefly,
896 conductance-displacement [G(X)] activation curves were calculated by dividing I_{MET}
897 (averaged across 2-4 presentations) by the driving force (HP – I_{MET} reversal potential, 0.2
898 mV) (Corns et al., 2014) and plotting G_{MET} against probe displacement (*X*). Probe
899 displacement as a function of driving voltage was calibrated off-line with a photodiode
900 (Songer and Eatock, 2013). G(X) curves were averaged across HCs and fitted with a
901 Boltzmann function (Eq. 1):

$$G_{MET}(X) = \frac{G_{max} - G_{min}}{1 + e^{(\frac{X_{1/2} - X}{S})}} + G_{min} \quad (1)$$

where G_{max} and G_{min} are maximum and minimum MET conductance, respectively, $X_{1/2}$ is displacement that evokes half-maximal G_{MET} and S is displacement corresponding to an e-fold rise in G_{MET}. We used the Boltzmann fits to calculate operating range (OR): displacement range corresponding to 10 - 90% of the response range, $G_{max} - G_{min}$.

We characterized transducer adaptation for responses at $X_{1/2}$, shown previously to reveal both fast and slow components of adaptation in mouse utricular hair cells (Vollrath and Eatock 2003). To reduce noise, current responses were averaged (*n* usually 3) and low-pass filtered at 1.5 kHz. Fast and slow adaptation components were estimated from double-exponential fits of the first 300 ms of the step response (Eq. 2). Deviation of those fits at the onset response signaled a very fast transducer adaptation component, which was separately estimated with a single-exponential fit of the first 1.5 ms of the response (Eq. 3).

$$I(t) = A_{\mathrm{f}} e^{-\frac{t}{\tau_f}} + A_{\mathrm{s}} e^{-\frac{t}{\tau_s}} + I_{\mathrm{ss}} \quad (2)$$

$$I(t) = A_{\mathrm{vf}} e^{-\frac{t}{\tau_{vf}}} + I_{\mathrm{ss}} \quad (3)$$

Here τ_{vf}, τ_f and τ_s are the very short (1 ms or less), short (from 1 to 10 ms) and long (>10 ms) time constants, respectively; A_{vf}, A_f and A_s are the amplitudes of the corresponding exponential terms; and I_{SS} is the steady-state current. All HCs had a very fast or fast component or both; some lacked a slow component that was detectable in the 400-ms step.

We calculated extent of adaptation (% decay) at $X_{1/2}$ as follows (Eq. 4):

931 $$Extent\ of\ adaptation = \left(\frac{I_{\ peak} - I_{ss}}{I_{peak} - I_0}\right) \times 100 \quad (4)$$

932

933 where I_0, I_{peak}, and I_{SS} are pre-step, steady-state, and peak currents, respectively.

934

935 In mouse utricular HCs, the dominant voltage-gated currents are carried by outwardly
936 rectifying K_V channels (Martin et al., 2023). By the end of the first postnatal week, these
937 currents provide distinctive electrophysiological signatures in type I and type II mouse
938 utricular HCs, which include more negatively activating K^+ currents and more negative
939 resting potentials for type I HCs (Rüsch and Eatock, 1996; Rüsch et al., 1998). To
940 characterize the voltage dependence of the currents, we applied families of iterated test
941 voltage steps (400 ms duration) from holding potentials of –74 mV (type I HCs) and –64
942 mV (type II HCs). The different holding potentials reflect the difference in resting potentials
943 of the two HC types. Steady-state voltage dependence was measured by constructing
944 conductance-voltage [G(V)] relations from tail currents, measured 1 ms after the 400-ms
945 test voltage steps, at a common membrane voltage of –39 mV (chosen to reduce
946 contamination of tail currents by HCN currents). Tail current was converted to "tail
947 conductance" by dividing by driving force (V_m – V_{rev}), where V_{rev} is approximated by the
948 K^+ equilibrium potential (–84 mV in our solutions). Tail conductance was plotted against
949 the iterated test step voltage and fit with the Boltzmann function:

950

951 $$G(V) = \frac{G_{max} - G_{min}}{1 + e^{(V_{1/2} - V)/S)}} + G_{min} \ (5)$$

952

953 where $V_{1/2}$ is the voltage of half-maximal activation and S is the voltage change over
954 which G changes e-fold at voltages negative to $V_{1/2}$. Voltage was corrected for voltage
955 errors caused by residual R_S and for the liquid junction potential by subtracting 4 mV.
956 Input resistance (R_{in}) was estimated from current clamp data as the slope of a linear
957 regression of the V_m(I) relation for small currents around resting potential.

958

959 **Imaging of afferent terminal arbors in mouse utricle (Figure 6)**

960 To investigate whether afferent receptive fields (terminal arbors) were disrupted by the
961 lack of bundle reversal in the lateral extrastriola (LES), we recorded in whole-cell mode
962 from calyces near the LES-striolar border. To label the terminal arbors for imaging, we
963 included Alexa Fluor 594 (#A10438 Thermo Fisher Scientific) instead of sulforhodamine
964 in the pipette solution (50 micromolar). After whole-cell recording was achieved, we
965 waited 20 min as the fluorescent pipette solution diffused into the calyx and throughout
966 the terminal arbor, then removed the pipette and fixed the utricular epithelium with 4%
967 paraformaldehyde for 10 min at room temperature (~22°). Fixed utricles were immersed
968 in blocking buffer (PBS with 4% normal donkey serum and 0.2% triton) then treated with
969 primary antibodies diluted with blocking buffer overnight at 4°C. Primary antibodies were:
970 mouse monoclonal anti-βII spectrin (1:500; BD Transduction, #612562) , to label hair
971 bundles and show the location of the kinocilium by absence of label; rabbit polyclonal
972 anti-calbindin (1:250; Invitrogen, #711443) to label the striola and juxtastriola (Leonard
973 and Kevetter, 2002). Specimens were then washed extensively and incubated with
974 secondary antibodies conjugated with fluorescent proteins (donkey anti-mouse or rabbit
975 IgG (H + L) antibody, ThermoFisher Scientific) for 1 hr at 4°C. Stained specimens were
976 mounted whole in mounting medium (Vector Laboratories, #H-1500), imaged with
977 spinning-disc confocal microscopy (Marianas SDC 3i), and analyzed with Adobe
978 Photoshop 2021 and FluoRender (ver. 2.26.3).
979
980 **Measurement of excitability from mouse utricular afferents (Figure 8)**
981 To document excitability of afferents in the LES, we recorded from calyces in whole-cell
982 current clamp mode, injected current steps and noted the thresholds for spiking and the
983 firing patterns. Most LES afferents are dimorphic, forming both calyces and boutons on
984 type I and II HCs, respectively. We rejected calyces with resting potentials less negative
985 than –50 mV. We evoked spikes with current steps to determine if afferents had step-
986 evoked firing patterns consistent with expected zonal patterns of spiking regularity in
987 mammalian vestibular epithelia (Goldberg et al., 1990; Iwasaki et al., 2008; Kalluri et al.,
988 2010). Families of 500-ms current steps were applied from zero-current potential,
989 beginning at –200 pA and incremented by 50 pA. Threshold current (I_{thresh}) was taken as
990 the minimum current (±50 pA) required to evoke any spikes.

991

992 We classified neuronal firing patterns according to the number of spikes evoked by a 400-
993 ms step at $I_m = 3\times I_{thresh}$ (Ono et al., 2020): a pattern of 1-2 spikes at step onset was
994 considered 'transient'; if more spikes were evoked, the pattern was 'sustained'. These
995 patterns have been associated with the mechanisms that give rise to well-known
996 differences in the regularity of firing across zones. The transient step-evoked pattern is
997 associated with striolar, irregular afferents and the sustained step-evoked pattern with
998 extrastriolar, regular afferents. The difference in step-evoked firing patterns is attributed
999 to zonal differences in expression of K_V channels that influence spike regularity (Iwasaki
1000 et al., 2008; Kalluri et al., 2010) and, more importantly, encoding strategy of afferent fibers
1001 (Jamali et al., 2019).
1002

1003 **Data analysis and statistics – mouse electrophysiology (Figures 2-4, Figure 8)**
1004 Data analysis, statistical tests, curve fitting and graphing were done with OriginPro (2022;
1005 OriginLab, Northampton, MA), Clampfit (Molecular Probes) and Matlab (Mathworks,
1006 Natick, MA). For samples that had homogeneous variance, significance was tested with
1007 either a two-tailed t-test or a one-way ANOVA with post-hoc Tukey test. When samples
1008 had unequal variance, we used either Welch's t-test or Kruskal-Wallis ANOVA with post-
1009 hoc Mann-Whitney U test. For significant differences ($p < 0.05$), we calculated effect size
1010 with Hedge's g equation. For non-significant (NS) differences, we calculated statistical
1011 power *post hoc* (OriginPro 2022) and these values are entered in tables along with p-
1012 values.
1013

1014 **Quantification of vestibular reflexes in mice (Figures 11-12)**
1015 We tested the angular vestibulo-ocular reflex (aVOR), the optokinetic reflex (OKR), and
1016 the otolith vestibulo-ocular reflex (off-vertical axis rotation, OVAR). Specifically, aVOR
1017 tests semicircular canal function, whereas OVAR tests otolith function. For completeness
1018 we also tested each animal's OKR as a control of the integrity of visuo-motor function.
1019

1020 **aVOR and OKR.** Surgical techniques and experimental setup have been previously
1021 described (Beraneck and Cullen, 2007). Eye movement data were collected using an

1022 infrared video system (ETL-200, ISCAN system). The rotational velocity of the turntable
1023 (head velocity) was measured using a MEMS sensor (MPU-9250, SparkFun Electronics).
1024 Eye movements during the OKR were evoked by sinusoidal rotations of a visual surround
1025 (vertical black and white stripes, visual angle width of 5°) placed around the turntable at
1026 frequencies 0.2, 0.4, 0.8, 1, 2, and 3 Hz with peak velocities of ±16°/s. To record VOR
1027 responses, the turntable was rotated at sinusoidal frequencies 0.2, 0.4, 0.8, 1, 2, and 3
1028 Hz with peak velocities of ±16°/s in both light and dark. In the light condition, the visual
1029 surround remained stationary, whereas, in the dark condition, both the visual surround
1030 and turntable rotated in phase and the surroundings was made dark. Head and eye
1031 movement signals were low-passed filtered at 125 Hz and sampled at 1 kHz. Eye position
1032 data were differentiated to obtain velocity traces. Cycles of data with quick phases were
1033 excluded from the analysis. Least-square optimization determined the VOR and OKR
1034 gains, and phases plotted as mean ± standard error of the mean (SEM) against all
1035 frequencies for all mice.
1036
1037 **OVAR.** Techniques employed for measurement of eye movements during OVAR in alert
1038 mice were described elsewhere (Beraneck et al., 2012). Briefly, recordings made after
1039 fixating mice on a rotating platform, which was tilted 17° with respect to the ground. The
1040 platform speed was increased from 0 to 50°/s in 500 ms and maintained its constant
1041 velocity for 72 s (10 complete rounds) before being stopped. Eye movements were
1042 measured using the same Infrared video system (ETL-200, ISCAN system) used for
1043 angular VOR and OKR recordings. Quick phases were identified as previously described
1044 and excluded from subsequent analysis. We then estimated the time constant of the
1045 OVAR slow-phase eye velocity response decay, as well as the amplitude and phase of
1046 its sinusoidal modulation using a linear regression approach.
1047
1048 **Mouse swimming assessment**
1049 A large container (26.25 × 16.25 × 14.38′) was filled with water (24–26°C) at the height
1050 of at least 15 cm. The mouse was placed into the water and observed for up to 1 min. Its
1051 performance was rated using the following scale (Hardisty-Hughes et al., 2010):
1052 0 = swims, body elongated, and tail propels in flagella-like motion.

1053 1 = immobile floating.
1054 2 = underwater tumbling.
1055 In a time-to-rescue trial, if an animal exhibited distressed swimming (underwater
1056 tumbling) before 60 seconds, the animal was rescued and time of rescue was marked. If
1057 not, the trial was marked as lasting 60 seconds.
1058
1059 **Mouse balance beam assessment**
1060 A 6-mm-wide and 40-cm-long beam was used for balance beam testing. The mice
1061 traversed 40 cm to a dark box. Walking speed was measured by recording the time the
1062 mouse took to reach the goal box from the opposite end of the beam. Mice were scored
1063 "time out" if they failed to reach the endpoint in 2 min.
1064
1065 **Air Righting, Tailing Hanging, and Contact Inhibition of Righting Tests**
1066 *Air Righting Test*
1067 The mouse was picked up by the tail and lowered into a container (size of container?) so
1068 that all four feet touched the bottom. The container was quickly inverted at a height of
1069 30–40 cm so mouse fell supine onto a foam cushion below. How the mouse landed was
1070 observed and rated as below (Rabbath et al., 2001):
1071 0 = the animal lands on its feet (normal).
1072 1 = the animal lands on its side (mild deficit).
1073 2 = the animal lands on its back (severe deficit).
1074
1075 *Tail Hanging Test*
1076 The animal was picked up by the tail and lowered to an even surface, and its posture
1077 rated using the following scale (Rabbath et al., 2001):
1078 0 = straight body posture with extension of forelimbs toward the earth (normal).
1079 1 = slightly bending the body ventrally (intermediate response).
1080 2 = persistently bending the body (severe response).
1081
1082 *Contact Inhibition of Righting Test*
1083 The mouse was picked up by the tail and lowered into a small container so that all four

1084 feet were in contact with the bottom, then the top of the container closed in contact with
1085 the mouse's back. The container was then quickly inverted so that the mouse became
1086 supine while the surface remains in contact with the soles of the mouse's feet. The
1087 mouse's reflex was rated using the following scale (Rabbath et al., 2001):
1088 0 = animal rights successfully (normal).
1089 1 = partial righting (intermediate response).
1090 2 = complete loss of righting (severe response).
1091
1092 **Quantification of Tremor during Resting Head Movement (Supplemental fig. 2)**
1093 Mice were placed in a cylinder (9 cm diameter and 21.5 cm height) that limited their
1094 motion, so mice maintained their steady posture. Head movements in six dimensions
1095 were recorded for 2 minutes using a miniature head motion sensor (MPU-9250,
1096 SparkFun Electronics, Niwot, CO, United States) affixed on the top of the skull, which
1097 comprises a three-dimensional (3D) accelerometer (measures linear acceleration;
1098 fore/aft, lateral, and vertical) and 3D gyroscope (measures angular velocity: roll, pitch,
1099 and yaw). Data was acquired at 200 Hz using windows-based CoolTerm software. We
1100 then computed the power spectral densities (pwelch function, MATLAB, MathWorks)
1101 using Welch's averaged periodogram with nfft = 4,096 and a Bartlett window (4,096 ms
1102 duration) for all six dimensions of movement.
1103
1104 **Data analysis and statistics – mouse behavior (Figures 11-12)**
1105 Data are reported as the mean ± SEM. Nonparametric Mann-Whitney U-test was
1106 performed to test significance for time to traverse (balance beam) and time to rescue
1107 (swimming) between two groups. Two-way repeated-measures ANOVA followed by
1108 Bonferroni post hoc comparison tests was used for the VOR data across frequencies. For
1109 power spectra analysis we used an independent sample permutation test to test
1110 significant differences between the two groups. Prism 9 (GraphPad) or MATLAB was
1111 used for statistical analyses. The same independent sample permutation test was also
1112 used to test significance for bias and gain of OVAR responses.
1113
1114 **Zebrafish strains and husbandry**

1115 Zebrafish (*Danio rerio*) were grown at 30 °C using a 14 hr light, 10 hr dark cycle. Larvae
1116 were raised in E3 embryo medium (5 mM NaCl, 0.17 mM KCl, 0.33 mM $CaCl_2$, and
1117 0.33 mM $MgSO_4$, pH 7.2). Larvae were examined at 5-6 days post fertilization (dpf). The
1118 following previously established mutant and transgenic zebrafish strains were used in this
1119 study: *gpr156*^{idc15}, *emx2*^{idc5} (Jiang et al., 2017; Kindt et al., 2021),
1120 *Tg(myo6b:memGCaMP6s*^{idc1} (Kindt et al., 2021). For comparisons, *emx2* mutants were
1121 compared to wild-type or *emx2*$^{+/-}$ animals. *Gpr156* mutants were compared to *gpr156*$^{+/-}$
1122 animals. Zebrafish work was performed at the National Institute of Health (NIH) and
1123 approved by the Animal Use Committee at the NIH under animal study protocol #1362-
1124 13.
1125
1126 **Zebrafish immunofluorescence and imaging (Figures 5, Figures 9-10)**
1127 Immunohistochemistry was performed on whole larvae at 5 dpf. Whole larvae were fixed
1128 with 4% paraformaldehyde in PBS at 4°C for 3.5 hr. For pre- and post-synaptic labeling
1129 all wash, block and antibody solutions were prepared with 0.1% Tween in PBS (PBST).
1130 For Emx2 labeling performed on sparse afferent labeling (see below) all wash, block and
1131 antibody solutions were prepared with PBS + 1% DMSO, 0.5% Triton-X100, 0.1% Tween-
1132 20 (PBDTT). After fixation, larvae were washed 4 × 5 min in PBST or PBDTT. For synaptic
1133 labeling, larvae were permeabilized with Acetone. For this permeabilization larvae were
1134 washed for 5 min with H_2O. The H_2O was removed and replaced with ice-cold acetone
1135 and placed at −20°C for 5 min, followed by a 5 min H_2O wash. The larvae were then
1136 washed for 4 × 5 min in PBST. For all immunostains larvae were blocked overnight at 4°C
1137 in blocking solution (2% goat serum, 1% bovine serum albumin, 2% fish skin gelatin in
1138 PBST or PBDTT). Larvae were then incubated in primary antibodies in antibody solution
1139 (1% bovine serum albumin in PBST or PBDTT) overnight, nutating at 4°C. The next day,
1140 the larvae were washed for 4 × 5 min in PBST or PBDTT to remove the primary antibodies.
1141 Secondary antibodies in antibody solution were added and larvae were incubated for 2
1142 hrs at room temperature, with minimal exposure to light. Secondary antibodies were
1143 washed out with PBST or PBDTT for 4 × 5 min. Larvae were mounted on glass slides
1144 with Prolong Gold (ThermoFisher Scientific) using No. 1.5 coverslips. Primary antibodies
1145 used were:

1146 Rabbit anti-Myo7a (Proteus 25-6790; 1:1000)
1147 Mouse anti-Ribeye b (IgG2a) (Sheets et al., 2011)
1148 Mouse anti-pan-MAGUK (IgG1) (Millipore MABN7; 1:500)
1149 Mouse anti-Myo7a (DSHB 138-1; 1:500)
1150 Rabbit anti-Emx2 (Trans Genic KO609; 1:250).
1151 The following secondaries were used at 1:1000 for synaptic labeling: goat anti-rabbit
1152 Alexa 488, goat anti-mouse IgG2a Alexa 546, goat anti-mouse IgG1 Alexa 647, along
1153 with Alexa 488 Phalloidin (Thermofischer; #A-11008, #A-21133, #A-21240, #A12379).
1154 For Emx2 co-labeling the following secondaries were used at 1:1000: goat anti-mouse
1155 Alexa 488, and goat ant-rabbit Alexa 647, along with Alexa 488 Phalloidin (Thermofischer;
1156 #A12379, #A28175, #A27040).
1157 Fixed samples were imaged on an inverted Zeiss LSM 780 laser-scanning confocal
1158 microscope with an Airyscan attachment (Carl Zeiss AG, Oberkochen, Germany) using
1159 an 63 × 1.4 NA oil objective lens. Airyscan z-stacks were acquired every 0.18 µm. The
1160 Airyscan Z-stacks were processed with Zen Black software v2.1 using 2D filter setting of
1161 6.0. Experiments were imaged with the same acquisition settings to maintain consistency
1162 between comparisons. Processed imaged were further processed using Fiji.
1163
1164 **Zebrafish immunostain quantification (Figure 5, Figures 9-10)**
1165 Images were processed in ImageJ. Researcher was not blinded to genotype. Hair bundle
1166 orientation was scored relative to the midline of the muscle somites. HC number per
1167 neuromast were quantified based on Myo7a labeling and presence of a paired/complete
1168 synapse. For quantification of Emx2 labeling, HCs were scored as Emx2 positive if they
1169 labeled with both Emx2 and Myo7a. To quality as a ribbon or presynapse, the following
1170 minimum size filters were applied to images: Ribeye b: 0.025 μm^2, MAGUK: 0.04 μm^2. A
1171 complete synapse was comprised of both a Ribeye b and MAGUK puntca. An unpaired
1172 presynapse consisted of only a Ribeye b puntca, while an unpaired postsynapse
1173 consisted of only a MAGUK puncta. In each neuromast all HCs (~15 HC per neuromast)
1174 were examined for our quantifications.
1175
1176 **Zebrafish functional calcium imaging in hair bundles (Figure 5)**

1177 GCaMP6s-based calcium imaging in zebrafish hair bundles has been previously
1178 described (Lukasz and Kindt, 2018). Briefly, individual 5-6 dpf larvae were first
1179 anesthetized with tricaine (0.03% Ethyl 3-aminobenzoate methanesulfonate salt,
1180 SigmaAldrich). To restrain larvae, they were then pinned to a Sylgard-filled recording
1181 chamber. To suppress the movement, alpha-bungarotoxin (125 μM, Tocris) was injected
1182 into the heart. Larvae were then rinsed and immersed in extracellular imaging solution (in
1183 mM: 140 NaCl, 2 KCl, 2 $CaCl_2$, 1 $MgCl_2$ and 10 HEPES, pH 7.3, OSM 310 +/- 10) without
1184 tricaine. A fluid jet was used to mechanically stimulate the apical bundles of HCs of the
1185 A-P neuromasts of the primary posterior lateral-line. To stimulate the two orientations of
1186 HCs (A>P and P>A) a 500 ms 'push' was delivered. Larvae were rotated 180° to deliver
1187 a comparable 'push' stimulus to both the A>P and P>A HCs.
1188
1189 To image calcium-dependent mechanosensitive responses in apical hair bundles, a
1190 Bruker Swept-field confocal system was used. The Bruker Swept-field confocal system
1191 was equipped with a Rolera EM-C2 CCD camera (QImaging) and a Nikon CFI Fluor
1192 60× 1.0 NA water immersion objective. Images were acquired in 5 planes along the Z-
1193 axis at 0.5 μm intervals (hair bundles) at a 50 Hz frame rate (10 Hz volume rate). The 5
1194 plane Z-stacks were projected into one plane for image processing and quantification.
1195 The method to create spatial ΔF heatmaps has been described (Lukasz and Kindt, 2018).
1196 For GCaMP6s measurements, a circular ROI with a ~1.5 μm (hair bundles) diameter was
1197 placed on the center of each individual bundle. The mean intensity ($\Delta F/F_0$) within each
1198 ROI was quantified. F_0 represents the GCaMP6s intensity prior to stimulation. We
1199 examined the GCaMP6s signal in each hair bundle to determine its orientation. The
1200 GCaMP6s responses for each neuromast were averaged to quantify the magnitude of the
1201 A>P and P>A responses.
1202
1203 **Zebrafish sparse labeling of single afferents in the lateral-line (Figure 9)**
1204 To visualize the innervation pattern of single afferent neurons, a *neuroD1:tdTomato*
1205 plasmid was injected into zebrafish embryos at the 1-cell stage. This plasmid consists of
1206 a 5kb minimal promoter, *neurod1*, that drives tdTomato expression in lateral-line afferents
1207 (Ji et al., 2018). This plasmid was pressure at a concentration of 30 ng/μl. At 3 dpf larvae

1208 were anesthetized with 0.03% ethyl 3-aminobenzoate methanesulfonate (Tricaine), to
1209 screen for tdTomato expression. Larvae were screened for mosaic expression of
1210 tdTomato expression in the lateral-line afferents using a Zeiss SteREO Discovery V20
1211 microscope (Carl Zeiss) with an X-Cite 120 external fluorescent light source (EXFO
1212 Photonic Solutions Inc). After selecting larvae with tdTomato expression, larvae were
1213 prepared for immunostaining at 5 dpf, and imaged as outlined above.

1214

1215 **Zebrafish data analysis and statistics**

1216 Statistical analyses and data plots were performed with Prism 9 (Graphpad, San Diego,
1217 CA). Values of data with error bars on graphs and in text are expressed as mean ± SEM
1218 unless indicated otherwise. All experiments were performed on a minimum of 3 animals,
1219 6 neuromasts (primary posterior lateral-line neuromasts with A-P orientations: L1-L5). For
1220 5-6 dpf larvae, each neuromast represents analysis from 12 to 20 HCs and 41–68
1221 synapses. All replicates are biological. No animals or samples were excluded from our
1222 analyses unless control experiments failed–in these cases all samples were excluded.
1223 No randomization or blinding was used for our animal studies. Where appropriate, data
1224 was confirmed for normality using a D'Agostino-Pearson normality test. Statistical
1225 significance between conditions was determined by an unpaired *t* -test.

1226

1227

1228 **REFERENCES**

1229

1230 **Beraneck, M., Bojados, M., Le Seac'h, A., Jamon, M. and Vidal, P. P.** (2012). Ontogeny of
1231 mouse vestibulo-ocular reflex following genetic or environmental alteration of gravity
1232 sensing. *PLoS One* **7**, e40414.
1233 **Chitnis, A. B., Nogare, D. D. and Matsuda, M.** (2012). Building the posterior lateral line system
1234 in zebrafish. *Dev Neurobiol* **72**, 234-255.
1235 **Chou, S. W., Chen, Z., Zhu, S., Davis, R. W., Hu, J., Liu, L., Fernando, C. A., Kindig, K., Brown, W.**
1236 **C., Stepanyan, R., et al.** (2017). A molecular basis for water motion detection by the
1237 mechanosensory lateral line of zebrafish. *Nature communications* **8**, 2234.
1238 **Corns, L. F., Johnson, S. L., Kros, C. J. and Marcotti, W.** (2014). Calcium entry into stereocilia
1239 drives adaptation of the mechanoelectrical transducer current of mammalian cochlear
1240 hair cells. *PNAS* **111**, 14918-14923.
1241 **Cullen, K. E.** (2019). Vestibular processing during natural self-motion: implications for
1242 perception and action. *Nat Rev Neurosci* **20**, 346-363.
1243 **Daigle, T. L., Madisen, L., Hage, T. A., Valley, M. T., Knoblich, U., Larsen, R. S., Takeno, M. M.,**
1244 **Huang, L., Gu, H., Larsen, R., et al.** (2018). A Suite of Transgenic Driver and Reporter
1245 Mouse Lines with Enhanced Brain-Cell-Type Targeting and Functionality. *Cell* **174**, 465-
1246 480 e422.
1247 **Deans, M. R.** (2013). A balance of form and function: planar polarity and development of the
1248 vestibular maculae. *Seminars in cell & developmental biology* **24**, 490-498.
1249 **Deans, M. R., Antic, D., Suyama, K., Scott, M. P., Axelrod, J. D. and Goodrich, L. V.** (2007).
1250 Asymmetric distribution of prickle-like 2 reveals an early underlying polarization of
1251 vestibular sensory epithelia in the inner ear. *J Neurosci* **27**, 3139-3147.
1252 **Denman-Johnson, K. and Forge, A.** (1999). Establishment of hair bundle polarity and
1253 orientation in the developing vestibular system of the mouse. *J Neurocytol* **28**, 821-835.
1254 **Eatock, R. A. and Songer, J. E.** (2011). Vestibular hair cells and afferents: two channels for head
1255 motion signals. *Annu Rev Neurosci* **34**, 501-534.
1256 **Fernandez, C., Goldberg, J. M. and Abend, W. K.** (1972). Response to static tilts of peripheral
1257 neurons innervating otolith organs of the squirrel monkey. *J Neurophysiol* **35**, 978-987.
1258 **Fernandez, C., Goldberg, J. M. and Baird, R. A.** (1990). The vestibular nerve of the chinchilla. III.
1259 Peripheral innervation patterns in the utricular macula. *J Neurophysiol* **63**, 767-780.
1260 **Flock, A.** (1964). Structure of the Macula Utriculi with Special Reference to Directional Interplay
1261 of Sensory Responses as Revealed by Morphological Polarization. *J Cell Biol* **22**, 413-431.
1262 **Goldberg, J. M.** (1991). The vestibular end organs: morphological and physiological diversity of
1263 afferents. *Current opinion in neurobiology* **1**, 229-235.
1264 **----** (2000). Afferent diversity and the organization of central vestibular pathways. *Exp Brain Res*
1265 **130**, 277-297.
1266 **Goldberg, J. M., Desmadryl, G., Baird, R. A. and Fernandez, C.** (1990). The vestibular nerve of
1267 the chinchilla. V. Relation between afferent discharge properties and peripheral
1268 innervation patterns in the utricular macula. *J Neurophysiol* **63**, 791-804.

1269 **Gonzalez-Garrido, A., Pujol, R., Lopez-Ramirez, O., Finkbeiner, C., Eatock, R. A. and Stone, J. S.**
1270 (2021). The Differentiation Status of Hair Cells That Regenerate Naturally in the
1271 Vestibular Inner Ear of the Adult Mouse. *J Neurosci* **41**, 7779-7796.
1272 **Holley, M., Rhodes, C., Kneebone, A., Herde, M. K., Fleming, M. and Steel, K. P.** (2010). Emx2
1273 and early hair cell development in the mouse inner ear. *Dev Biol* **340**, 547-556.
1274 **Iwasaki, S., Chihara, Y., Komuta, Y., Ito, K. and Sahara, Y.** (2008). Low-voltage-activated
1275 potassium channels underlie the regulation of intrinsic firing properties of rat vestibular
1276 ganglion cells. *J Neurophysiol* **100**, 2192-2204.
1277 **Jacobo, A., Dasgupta, A., Erzberger, A., Siletti, K. and Hudspeth, A. J.** (2019). Notch-Mediated
1278 Determination of Hair-Bundle Polarity in Mechanosensory Hair Cells of the Zebrafish
1279 Lateral Line. *Current biology : CB* **29**, 3579-3587 e3577.
1280 **Jamali, M., Carriot, J., Chacron, M. J. and Cullen, K. E.** (2019). Coding strategies in the otolith
1281 system differ for translational head motion vs. static orientation relative to gravity. *eLife*
1282 **8**.
1283 **Ji, Y. R., Tona, Y., Wafa, T., Christman, M. E., Tourney, E. D., Jiang, T., Ohta, S., Cheng, H.,**
1284 **Fitzgerald, T., Fritzsch, B., et al.** (2022). Function of bidirectional sensitivity in the otolith
1285 organs established by transcription factor Emx2. *Nature communications* **13**, 6330.
1286 **Ji, Y. R., Warrier, S., Jiang, T., Wu, D. K. and Kindt, K. S.** (2018). Directional selectivity of
1287 afferent neurons in zebrafish neuromasts is regulated by Emx2 in presynaptic hair cells.
1288 *eLife* **7**.
1289 **Jiang, T., Kindt, K. and Wu, D. K.** (2017). Transcription factor Emx2 controls stereociliary bundle
1290 orientation of sensory hair cells. *eLife* **6**.
1291 **Jones, C., Qian, D., Kim, S. M., Li, S., Ren, D., Knapp, L., Sprinzak, D., Avraham, K. B.,**
1292 **Matsuzaki, F., Chi, F., et al.** (2014). Ankrd6 is a mammalian functional homolog of
1293 Drosophila planar cell polarity gene diego and regulates coordinated cellular orientation
1294 in the mouse inner ear. *Dev Biol* **395**, 62-72.
1295 **Kalluri, R., Xue, J. and Eatock, R. A.** (2010). Ion channels set spike timing regularity of
1296 mammalian vestibular afferent neurons. *J Neurophysiol* **104**, 2034-2051.
1297 **Kindig, K., Stepanyan, R., Kindt, K. S. and McDermott, B. M., Jr.** (2023). Asymmetric
1298 mechanotransduction by hair cells of the zebrafish lateral line. *Current biology : CB* **33**,
1299 1295-1307 e1293.
1300 **Kindt, K. S., Akturk, A., Jarysta, A., Day, M., Beirl, A., Flonard, M. and Tarchini, B.** (2021).
1301 EMX2-GPR156-Galphai reverses hair cell orientation in mechanosensory epithelia.
1302 *Nature communications* **12**, 2861.
1303 **Kozak, E. L., Palit, S., Miranda-Rodriguez, J. R., Janjic, A., Bottcher, A., Lickert, H., Enard, W.,**
1304 **Theis, F. J. and Lopez-Schier, H.** (2020). Epithelial Planar Bipolarity Emerges from Notch-
1305 Mediated Asymmetric Inhibition of Emx2. *Current biology : CB* **30**, 1142-1151 e1146.
1306 **Lein, E. S., Hawrylycz, M. J., Ao, N., Ayres, M., Bensinger, A., Bernard, A., Boe, A. F., Boguski,**
1307 **M. S., Brockway, K. S., Byrnes, E. J., et al.** (2007). Genome-wide atlas of gene expression
1308 in the adult mouse brain. *Nature* **445**, 168-176.
1309 **Leonard, R. B. and Kevetter, G. A.** (2002). Molecular probes of the vestibular nerve. I.
1310 Peripheral termination patterns of calretinin, calbindin and peripherin containing fibers.
1311 *Brain Res* **928**, 8-17.

1312 **Li, A., Xue, J. and Peterson, E. H.** (2008). Architecture of the mouse utricle: macular
1313 organization and hair bundle heights. *J Neurophysiol* **99**, 718-733.
1314 **Lindeman, H. H.** (1969). Regional differences in structure of the vestibular sensory regions. *The*
1315 *Journal of laryngology and otology* **83**, 1-17.
1316 **Lopez-Schier, H., Starr, C. J., Kappler, J. A., Kollmar, R. and Hudspeth, A. J.** (2004). Directional
1317 cell migration establishes the axes of planar polarity in the posterior lateral-line organ of
1318 the zebrafish. *Dev Cell* **7**, 401-412.
1319 **Lozano-Ortega, M., Valera, G., Xiao, Y., Faucherre, A. and Lopez-Schier, H.** (2018). Hair cell
1320 identity establishes labeled lines of directional mechanosensation. *PLoS biology* **16**,
1321 e2004404.
1322 **Maklad, A., Kamel, S., Wong, E. and Fritzsch, B.** (2010). Development and organization of
1323 polarity-specific segregation of primary vestibular afferent fibers in mice. *Cell and tissue*
1324 *research* **340**, 303-321.
1325 **Martin, H. R., Lysakowski, A. and Eatock, R. A.** (2023). The potassium channel subunit K(V)1.8
1326 (Kcna10) is essential for the distinctive outwardly rectifying conductances of type I and II
1327 vestibular hair cells. *bioRxiv*.
1328 **McInturff, S., Burns, J. C. and Kelley, M. W.** (2018). Characterization of spatial and temporal
1329 development of Type I and Type II hair cells in the mouse utricle using new cell-type-
1330 specific markers. *Biol Open* **7**.
1331 **Mirkovic, I., Pylawka, S. and Hudspeth, A. J.** (2012). Rearrangements between differentiating
1332 hair cells coordinate planar polarity and the establishment of mirror symmetry in
1333 lateral-line neuromasts. *Biol Open* **1**, 498-505.
1334 **Ono, K., Keller, J., Lopez Ramirez, O., Gonzalez Garrido, A., Zobeiri, O. A., Chang, H. H. V.,**
1335 **Vijayakumar, S., Ayiotis, A., Duester, G., Della Santina, C. C., et al.** (2020). Retinoic acid
1336 degradation shapes zonal development of vestibular organs and sensitivity to transient
1337 linear accelerations. *Nature communications* **11**, 63.
1338 **Rusch, A. and Eatock, R. A.** (1996). A delayed rectifier conductance in type I hair cells of the
1339 mouse utricle. *J Neurophysiol* **76**, 995-1004.
1340 **Rusch, A., Lysakowski, A. and Eatock, R. A.** (1998). Postnatal development of type I and type II
1341 hair cells in the mouse utricle: acquisition of voltage-gated conductances and
1342 differentiated morphology. *J Neurosci* **18**, 7487-7501.
1343 **Sheets, L., Trapani, J. G., Mo, W., Obholzer, N. and Nicolson, T.** (2011). Ribeye is required for
1344 presynaptic Ca(V)1.3a channel localization and afferent innervation of sensory hair cells.
1345 *Development* **138**, 1309-1319.
1346 **Simmons, D. D., Tong, B., Schrader, A. D. and Hornak, A. J.** (2010). Oncomodulin identifies
1347 different hair cell types in the mammalian inner ear. *J Comp Neurol* **518**, 3785-3802.
1348 **Songer, J. E. and Eatock, R. A.** (2013). Tuning and timing in mammalian type I hair cells and
1349 calyceal synapses. *J Neurosci* **33**, 3706-3724.
1350 **Tarchini, B.** (2021). A Reversal in Hair Cell Orientation Organizes Both the Auditory and
1351 Vestibular Organs. *Front Neurosci* **15**, 695914.
1352 **Ventura, C. M. and Kalluri, R.** (2019). Enhanced Activation of HCN Channels Reduces Excitability
1353 and Spike-Timing Regularity in Maturing Vestibular Afferent Neurons. *J Neurosci* **39**,
1354 2860-2876.

1355 **Vollrath, M. A. and Eatock, R. A.** (2003). Time course and extent of mechanotransducer
1356 adaptation in mouse utricular hair cells: comparison with frog saccular hair cells. *J*
1357 *Neurophysiol* **90**, 2676-2689.
1358 **Xue, J. and Peterson, E. H.** (2006). Hair bundle heights in the utricle: differences between
1359 macular locations and hair cell types. *J Neurophysiol* **95**, 171-186.
1360 **Zhou, X., Wang, L., Hasegawa, H., Amin, P., Han, B. X., Kaneko, S., He, Y. and Wang, F.** (2010).
1361 Deletion of PIK3C3/Vps34 in sensory neurons causes rapid neurodegeneration by
1362 disrupting the endosomal but not the autophagic pathway. *PNAS* **107**, 9424-9429.
1363

1364

1365

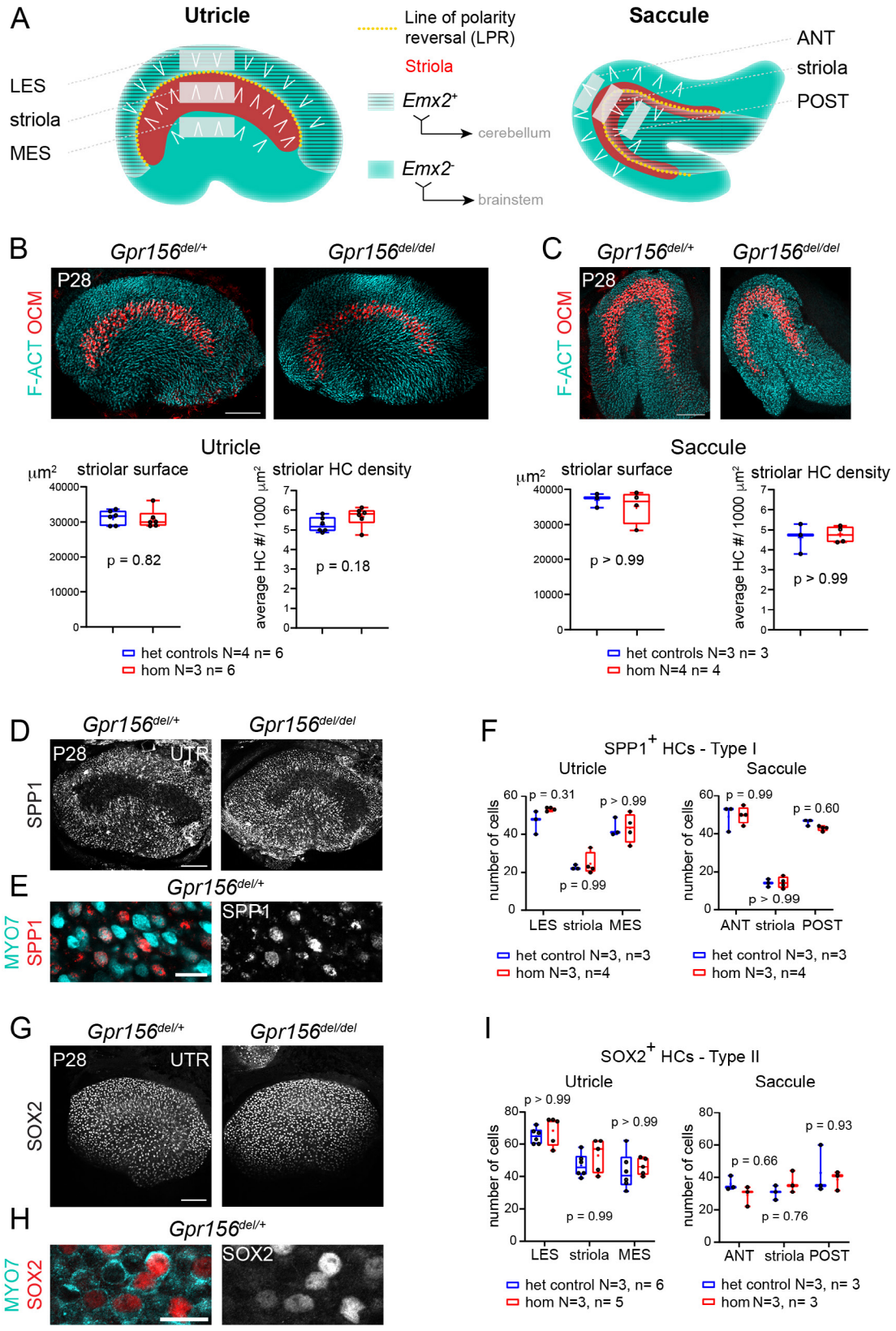
A
Utricle
Saccule
Line of polarity reversal (LPR)
Striola
Emx2+
cerebellum
Emx2-
brainstem
LES
striola
MES
ANT
striola
POST
B
Gpr156del/+
Gpr156del/del
P28
F-ACT OCM
C
Utricle
Saccule
striolar surface
striolar HC density
average HC #/ 1000 µm2
p = 0.82
p = 0.18
p > 0.99
p > 0.99
het controls N=4 n= 6
hom N=3 n= 6
het controls N=3 n= 3
hom N=4 n= 4
D
UTR
SPP1
E
MYO7
F
SPP1+ HCs - Type I
number of cells
p = 0.31
p > 0.99
p = 0.99
p = 0.99
p = 0.60
p > 0.99
LES striola MES
ANT striola POST
het control N=3, n=3
hom N=3, n=4
G
SOX2
H
I
SOX2+ HCs - Type II
p > 0.99
p > 0.99
p = 0.99
p = 0.93
p = 0.66
p = 0.76
het control N=3, n= 6
hom N=3, n= 5
het control N=3, n= 3
hom N=3, n= 3

1366

1367 **Figure 1. Normal striola and hair cell type organization in *Gpr156* mutants. A**)
1368 Diagrams showing general macular organization and the regions analyzed in **B-I** (LES,
1369 MES: lateral and medial extrastriola, respectively; ANT: anterior, POST: posterior). Each
1370 region is 130x50 μm in the utricle and 150x40 μm in the saccule. White chevrons indicate
1371 HC orientation. **B-C**) P28 utricles (**B**) and saccules (**C**) immunolabeled with oncomodulin
1372 (OCM) to reveal the striolar region and phalloidin to reveal F-actin (F-ACT)-rich hair
1373 bundles. Graphs report striolar surface area and striolar HC density based on OCM
1374 labeling and show no change in mutants compared to heterozygote littermate controls.
1375 All points are graphed along with 25-75% boxplots (external bars: minimum and maximum,
1376 internal bar: median, cross: mean). Mann-Whitney U test. **D-F**) P28 maculae
1377 immunolabeled with SPP1 to reveal type I HCs. Low magnification of the utricle (**D**), high
1378 magnification view showing SPP1 at the utricle HC neck (**E**), and quantification per region
1379 in utricle and saccule (**F**). **G-I**) P28 maculae immunolabeled with SOX2 to reveal type II
1380 HCs. Low magnification of the utricle (**G**), high magnification view showing SOX2 in the
1381 utricle HC nucleus (**H**), and quantification per region in utricle and saccule (**I**). **F**, **I:** 2-way
1382 ANOVA with Sidak's multiple comparisons. N, n: number of animals and HCs,
1383 respectively. UTR, utricle. Scale bars: 100 μm (**B**-**C**, **D**, **G**), 10 μm (**E**, **H**).
1384

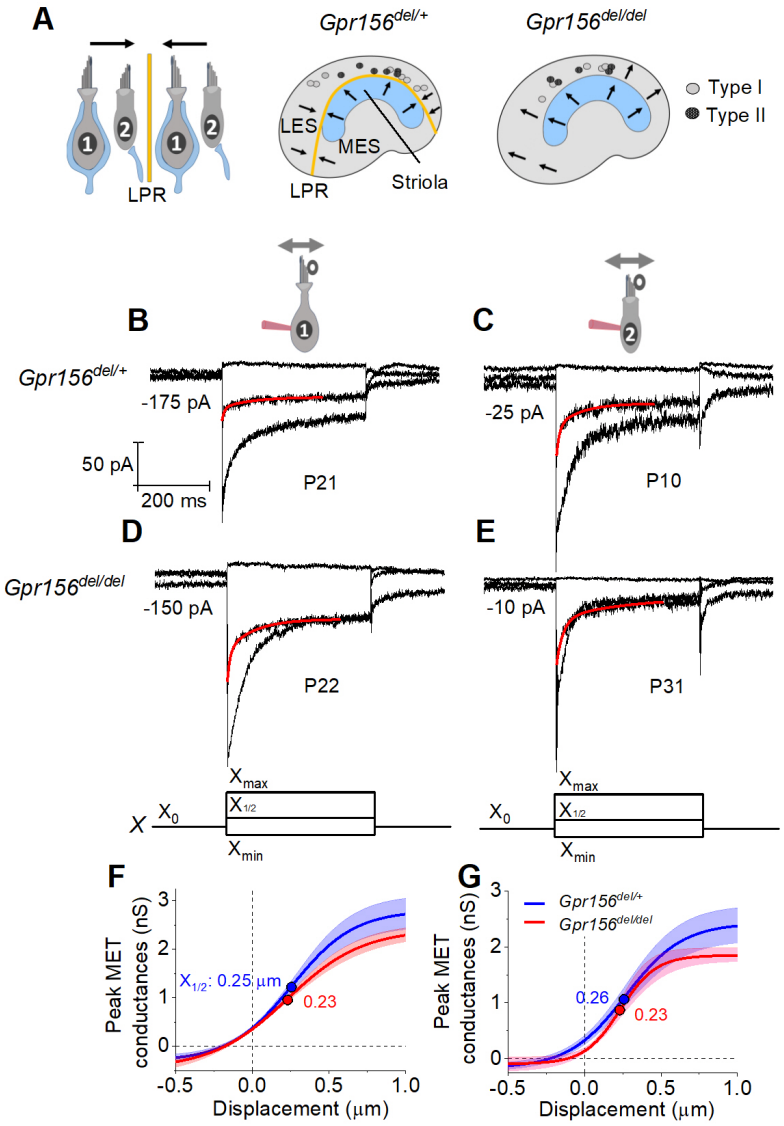

Figure 2. No effects of *Gpr156* deletion on mechanosensitivity were detected in LES hair cells. A) *Left,* Schematic showing hair cell types with normal reversed bundle polarity at the LPR. *Arrows*, Directions of hair bundle motion that produce a depolarizing receptor potential. *Right,* Maps of recordings from LES zone, lateral to the LPR in heterozygotes, and similar location in null mutants, but without bundle reversal (arrows). **B-E**) Exemplar I_{MET} recordings from voltage-clamped LES HCs of different type (I vs. II, columns) and genotype (het vs. null, rows), and ranging in age from P10 to P31. XY scales for all 4 are in **D**. Each panel shows I_{MET} current (average of 3 traces) evoked by 3 of many iterated bundle displacements (bottom of **D**, **E**): negatively and positively saturating stimuli (X_{min},

1396 X_{max}) plus a step to ~ $X_{1/2}$ (midpoint) of the operating range. *Red traces*, fits of current
1397 decay for step to $X_{1/2}$ with Eq. 2 or 3 (Methods). Voltage was clamped with the indicated
1398 holding currents at –94 mV (type I) and –84 mV (type II). **F,G**) *G(X*) relations from type I
1399 (**F**) and type II (**G**) HCs. G, was peak MET conductance taken at the onset of each of 20
1400 or 40 displacement steps (*X*), iterated by 100 nm or 35 nm, respectively, and averaged
1401 across 3 repeated stimulus families. *Mean ± SEM; n = 5-8 cells.* Fitted *G(X)* parameters
1402 are statistically similar for *Gpr156*$^{del/+}$ and *Gpr156*$^{del/del}$ HCs (see Table 2). *Filled circles,*
1403 $X_{1/2}$ values from fits. X_{max}: 1.1 to 1.3 micrometers. X_{min}; –0.2 to –0.45 micrometers.
1404

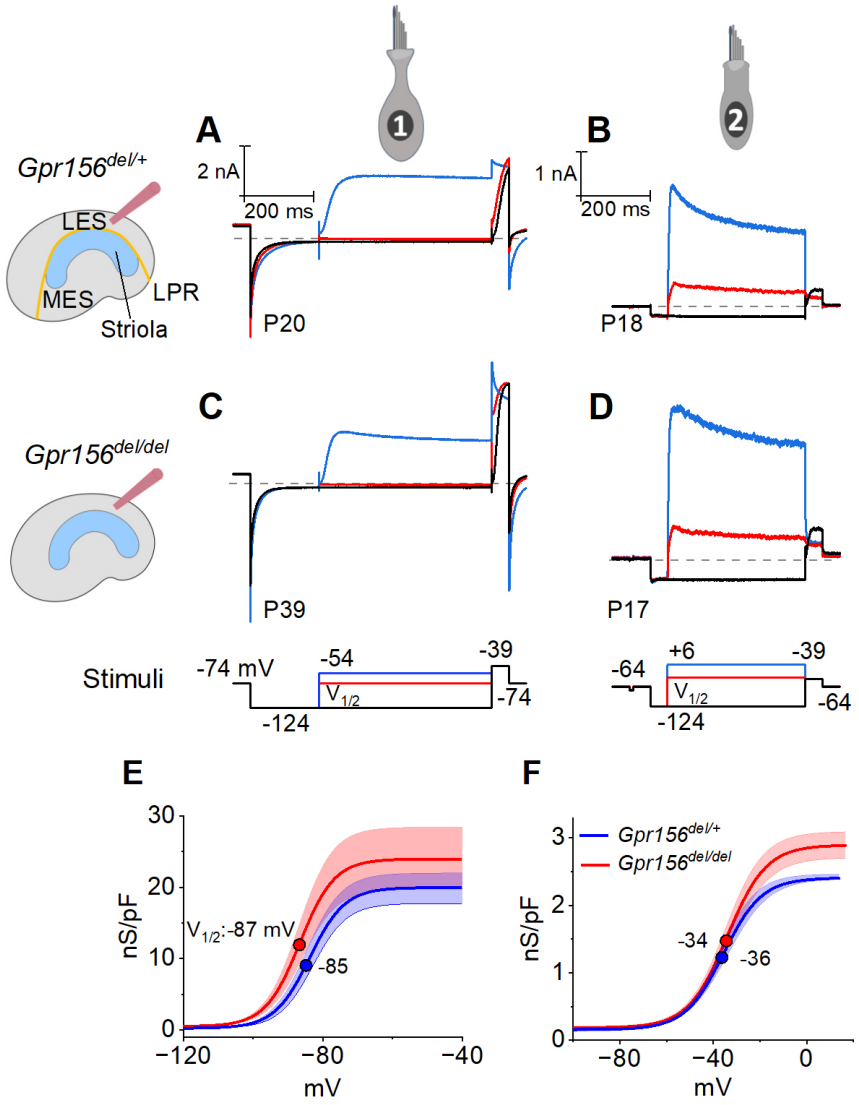

Figure 3. No effects of *Gpr156* deletion on basolateral voltage-dependent conductances were detected in LES HCs. A-D) Exemplar voltage-dependent currents from lateral extrastriolar (LES) type I (**A**, **C**) and type II (**B**, **D**) HCs of *Gpr156*$^{del/+}$ (**A**, **B**) and *Gpr156*$^{del/del}$ (**C**, **D**) utricles. There are significant differences between HC types, but these differences are seen in both *Gpr156*$^{del/+}$ (**A**, **B**) and *Gpr156*$^{del/del}$ utricles (**C**, **D**). A pre-pulse from holding potential to –124 mV shows the usual type I-type II difference in K^+ conductances at or near resting potential: the prepulse deactivates $g_{K,L}$ in type I cells (**A,C**), and activates a small inwardly rectifying current in type II cells (**B**, **D**). Following the pre-pulse, test steps were iterated in 5-mV increments from –124 mV to –54 mV (type

1416 I) or from –124 mV to +6 mV (type II), activating currents with very different time course
1417 and voltage dependence. **E**, **F**) G(V) relations measured from tail currents at the end of
1418 the iterated voltage steps show that $g_{K,L}$ activated positive to –114 mV (**E**) while type II
1419 delayed rectifying currents activated positive to –64 mV (**F**).

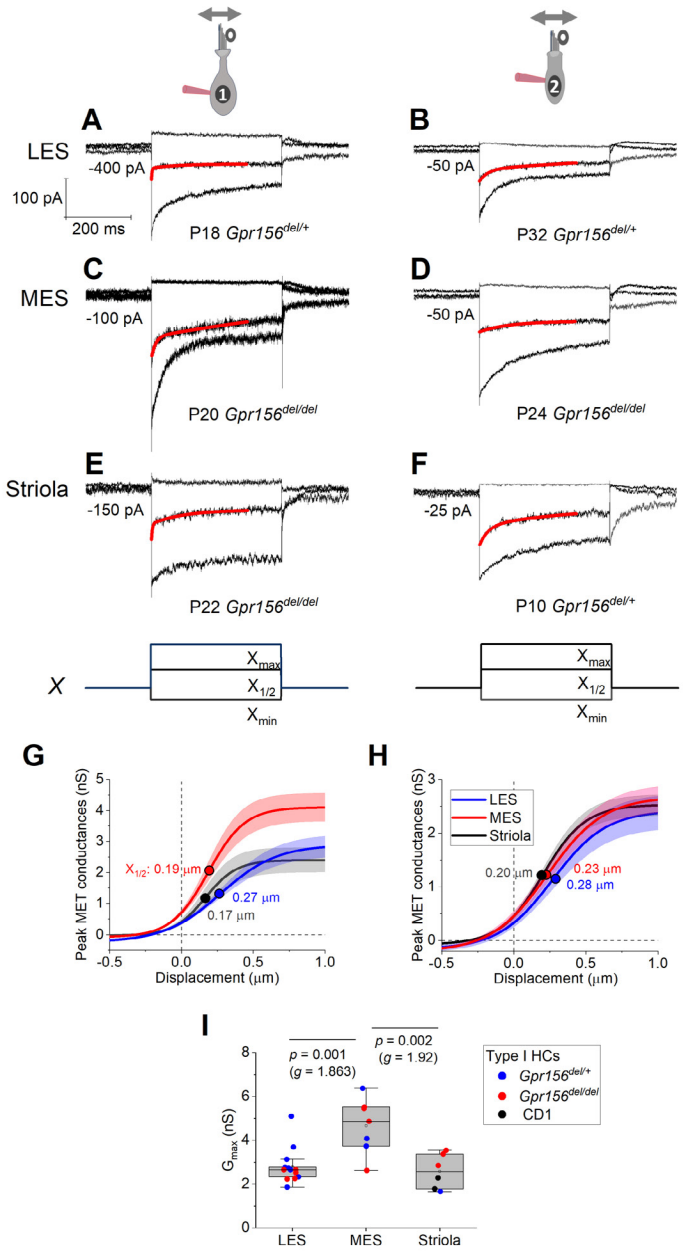

Figure 4. Displacement sensitivity and time course of step-evoked transduction currents in each zone were not strongly affected by Gpr156 deletion. A-F) Exemplar I_{MET} recordings from voltage-clamped HCs of different genotype, HC type (columns), and epithelial zone (rows). I_{MET} current families (averages of 3) evoked by 3 of many iterated bundle displacements (**E**, **F**, bottom): negatively and positively saturating stimuli plus the step closest to the midpoint ($X_{1/2}$) of the G(X) relation. X_{max}: 1.08 to 1.32 µm. X_{min}: –0.2 to –0.45 µm. *Red traces*, fits of current decay with Eq. 2 or 3 (Methods). Holding potentials,

1428 –94 mV (type I) and –84 mV (type II). **G-H**) Averaged peak (onset) $G_{MET}(X)$ relations for
1429 type I (**G**) and type II (**H**) HCs. Data from 5-9 HCs of each type were fitted with the
1430 Boltzmann functions, which were averaged to produce mean curves shown (± SEM). $X_{1/2}$
1431 values (filled circles) are given. **I**) Mean maximum G_{MET} of type I HCs was larger in MES
1432 than in LES or striola, but there was not a significant effect of genotype. *Black circles*, 2
1433 striolar type I HCs from CD1 mice.
1434

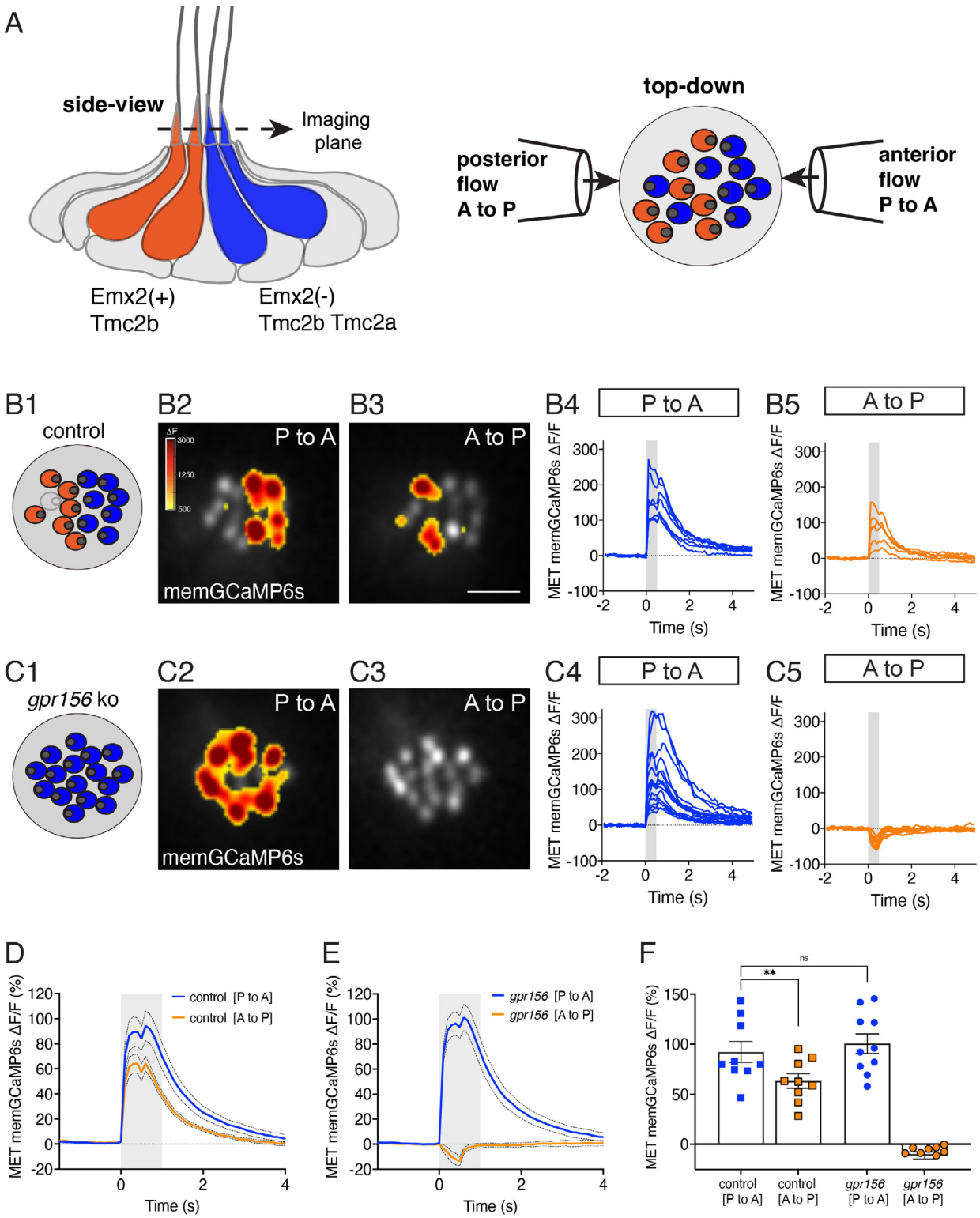

1435

1436 **Figure 5. Gpr156 impacted the mechanosensitive properties of lateral-line HCs. A**)
1437 Schematic on the left shows a lateral-line neuromast from the side. HCs that detect
1438 anterior (P to A) and posterior (A to P) flow are color coded in blue and orange

1439 respectively. Posterior HCs do not express Emx2 and rely primarily on the MET channel
1440 subunits Tmc2a and Tmc2b. In contrast, anterior HCs express Emx2 and rely primary on
1441 Tmc2b for mechanosensation. Schematic on the right shows a plane taken through the
1442 apical hair bundle plane, viewed top-down. The directional sensitivity of each HC is
1443 dictated by the location of the kinocilium, which is indicated by the circle on the side of
1444 each hair bundle. This apical plane is one used to monitor mechanosensitive-calcium
1445 signals in lateral-line hair bundles. The pipettes on each side of the hair bundles show the
1446 direction of flow delivered to stimulate the two populations of HCs. **B1**-**B5**) Representative
1447 example of evoked-mechanosensitive calcium signals in hair bundles of a control
1448 neuromast during a 500-ms anterior (**B2**) or a 500-ms posterior (**B3**) directed stimulus.
1449 Spatial patterns of GCaMP6s signals during stimulation (**B2**-**B3**) are colorized according
1450 to the ΔF heat map and superimposed onto a baseline GCaMP6s image. In **B1**, the
1451 colored circles indicate the respective hair bundle orientation observed from calcium
1452 imaging (A to P, orange; P to A, blue; no response, gray). ROIs were placed on each hair
1453 bundle to generate the ΔF/F GCaMP6s traces from individual hair bundles responding to
1454 P to A (**B4**) and A to P (**B5**) directed flow. **C1**-**C5**) Representative example of evoked-
1455 mechanosensitive calcium signals in hair bundles of a *gpr156* mutant neuromast during
1456 a 500-ms P to A (**C2**) or a 500-ms A to P (**C3**) directed stimulus. Spatial patterns of
1457 GCaMP6s signals during stimulation (**C2**-**C3**) are colorized according to the ΔF heat map
1458 in **B2** and superimposed onto a baseline GCaMP6s image. In **C1**, the colored circles
1459 indicate the respective hair bundle orientation observed from calcium imaging (P to A,
1460 blue). ROIs were placed on all hair bundle to generate the ΔF/F GCaMP6s traces from
1461 individual hair bundles during P to A (**C4**) and A to P (**C5**) directed stimuli. **D-F)**
1462 Quantification of the average increase in GCaMP6s per neuromast for P to A and A to P
1463 responding hair bundles. Traces in **D** and **E** show the average GCaMP6s response per
1464 neuromast in P to A and A to P hair-bundle populations (mean ± SEM is shown in **D**-**E**, n
1465 = 9 control and 10 *gpr156* neuromasts). The magnitude of the GCaMP6s data in **D**-**E** is
1466 plotted to compare the average GCaMP6s increase for P to A and A to P hair bundles for
1467 each neuromast in **F**. In control neuromasts, the GCaMP6s increase in the hair bundles
1468 responding to P to A flow was larger compared to those responding to A to P flow. In
1469 *gpr156* mutants the GCaMP6s increase in hair bundles responding to P to A flow was

1470 significantly larger than control A to P cells, but not different than control P to A cells. **P
1471 = 0.0043 and P = 0.561, paired and unpaired t-test respectively. Scale bar is 5 μm in **B3**.
1472

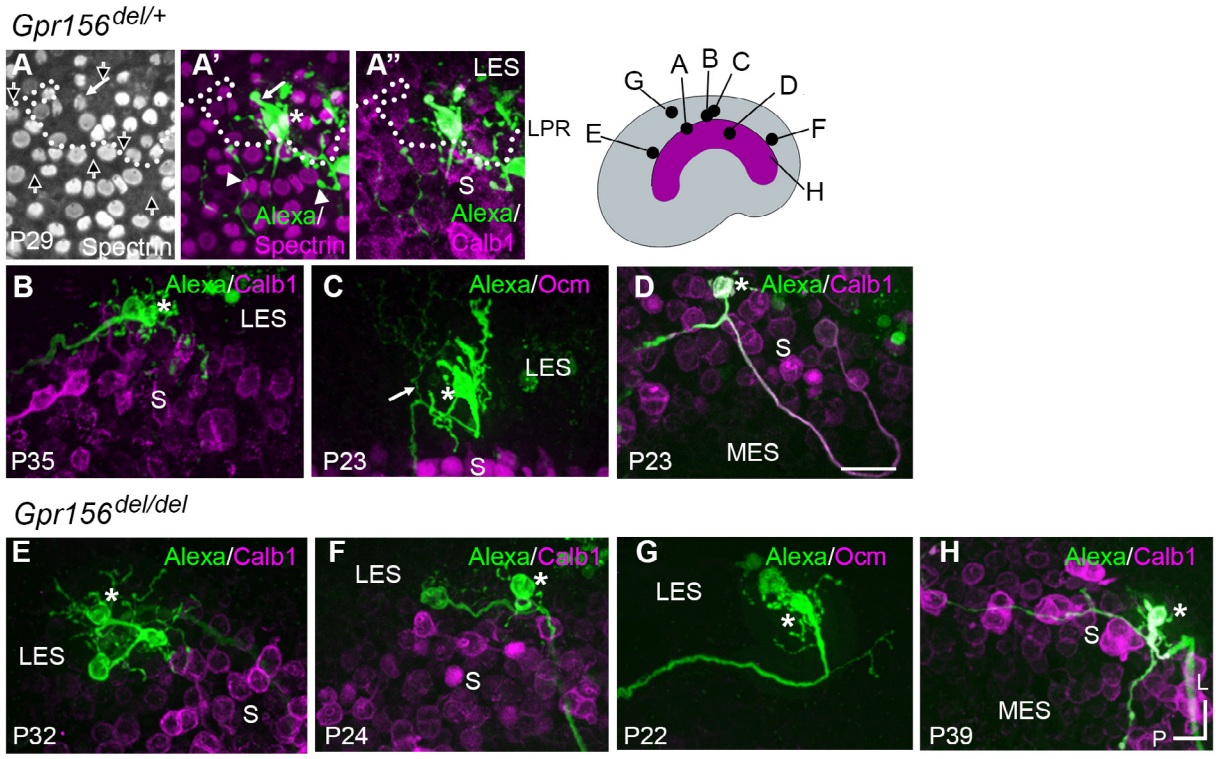

Figure 6. Afferent innervation patterns near the LES/S zone boundary were not substantially disturbed by *Gpr156* deletion. Afferent receptive fields (*green*) were labeled by diffusion of fluorescent dye (AlexaFluor) from whole-cell recording pipettes into calyces (*asterisks*) and throughout the terminal arbor, for (**A**-**D**) *Gpr156*$^{del/+}$ controls and (**E**-**H**) *Gpr156*$^{del/del}$ mutants. Counterstained with anti-calbindin (Calb1) antibody to show the striola (*magenta*). *Top right,* Schematic of the utricle with magenta striola; *black dots*, approximate location of each labelled calyx *shown*. All labeled afferents had a thick, medial-projecting neurite that branched to form up to 2 calyces and many bouton contacts. Anti-βII-spectrin labeling (**A**, **A'**) leaves an unlabeled hole where the kinocilium is, allowing determination of bundle orientation (*black arrows outlined in white, A*) and, in *Gpr156*$^{del/+}$ controls, the LPR (*dotted white line*). **A**) In one control afferent, the receptive field straddled the LPR (**A'**, **A''**), with 1 calyx on a type I HC in the LES (*white arrow*) and some boutons contacting type II HCs, as terminals or en passant, in the calbindin^{+} striola (*white arrowheads*). **B, C**) In all other fills, the labeled LES arbors innervated only LES HCs. **C,** *arrow*, A thin branch extended from the fiber below the epithelium (Supplemental video 1). **D**) A receptive field labeled by filling a striolar calyx included 2 calyces and some

1491 bouton endings, all restricted to the calbindin^{+} striola (this afferent is white because of the
1492 merge of AlexaFluor and calbindin stains). **E-G**) Afferent terminal fields of LES calyces
1493 from *Gpr156*$^{del/del}$ utricles largely remained in the calbindin^{-} region (LES). **H**) A striolar
1494 (calbindin^{+}) calyx in a *Gpr156*$^{del/del}$ mouse made multiple boutons entirely in the calbindin^{+}
1495 area (striola). Scale bar: 20 micrometers L, lateral; P, posterior.
1496

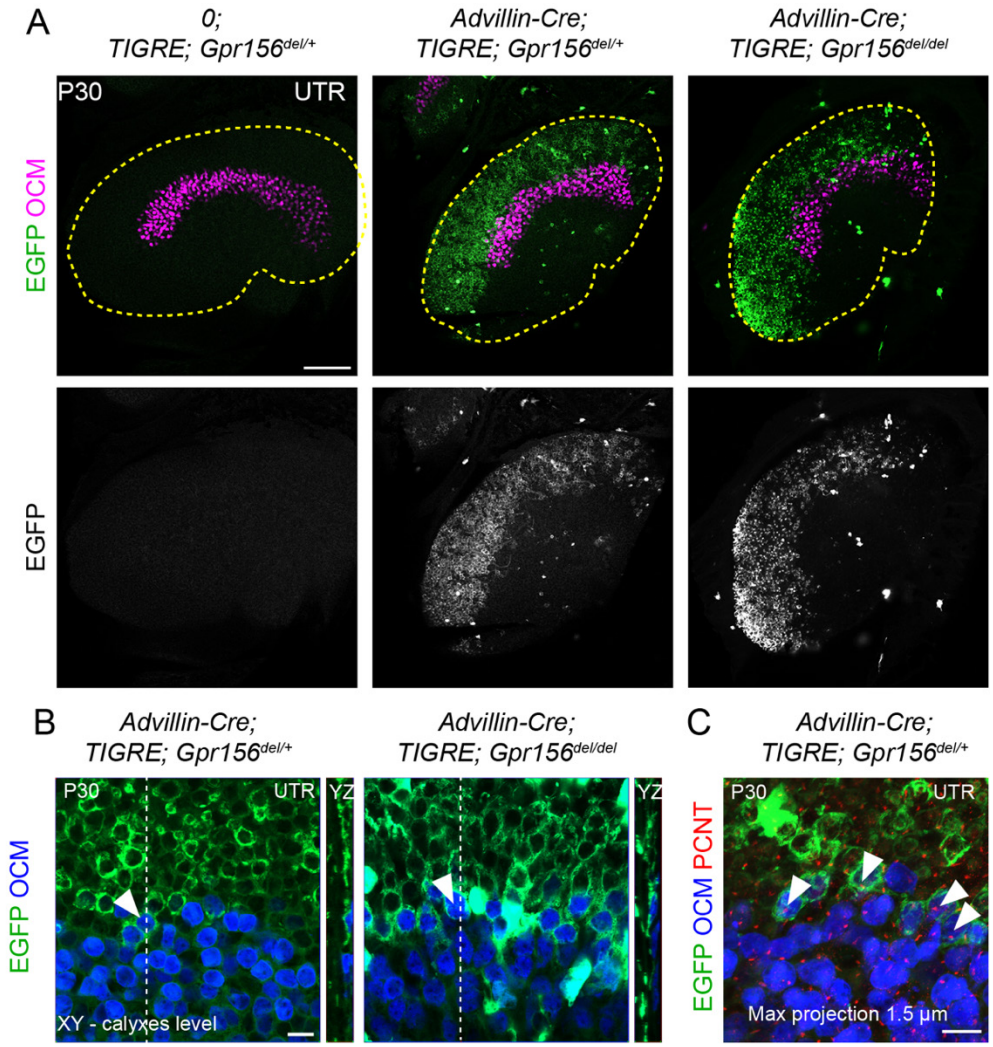

Figure 7. LES afferent innervation pattern was comparable for *Gpr156*$^{del/+}$ and *Gpr156*$^{del/del}$ utricles. A) P30 utricles where oncomodulin (OCM) labels striolar HCs and *Advillin*-positive afferents are labeled by EGFP in *Advillin-Cre; TIGRE; Gpr156* animals. *Advillin-Cre* neurons specifically innervated lateral HCs and orientation-based segregation was not altered in *Gpr156*$^{del/del}$ mutants. **B**) Close-up views at the LES-striola border (XY and YZ views). The vast majority of EGFP-positive HCs were in the the LES but *Advillin*-positive neurons also innervated OCM^{+} HCs in the lateral striola in both control and *Gpr156* mutants. **C**) Close-up view where basal bodies are labeled with pericentrin (PCNT) to reveal HC orientation (arrowheads). Lateral striolar HCs innervated by *Advillin* neurons were consistently oriented medially, showing that innervation from

1509 *Advillin* neurons strictly segregates with HC orientation, and not with striolar
1510 characteristics (OCM expression). Yellow dotted lines in A mark the outline of the utricle.
1511 Scale bars: 100 μm (A) 10 μm (B-C).
1512

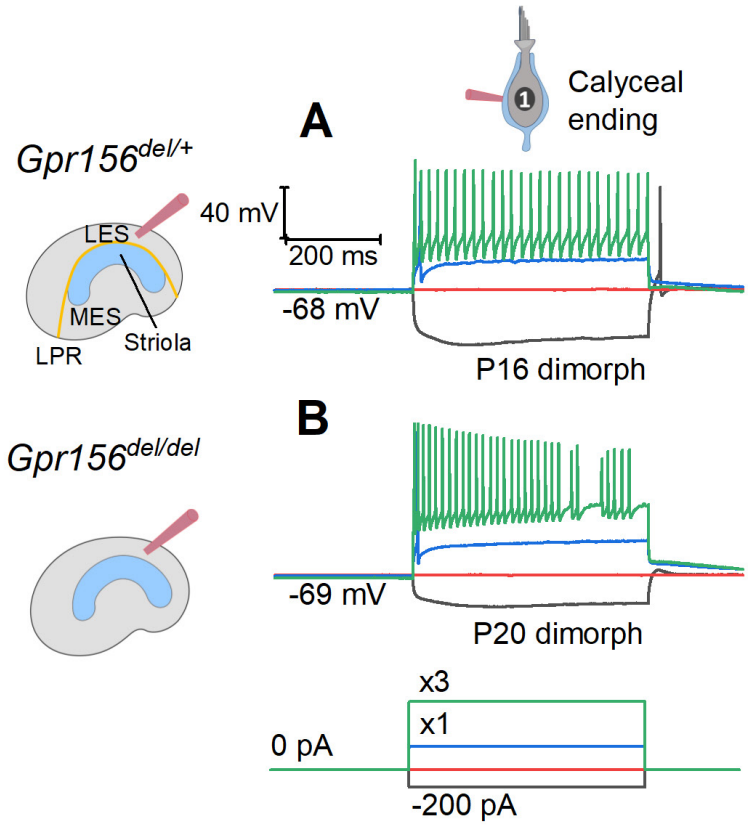

1513

1514

1515 **Figure 8. The excitability of LES afferents was not significantly affected by Gpr156**
1516 **deletion.** Exemplary voltage responses of control (**A**) and null (**B**) afferents to injected
1517 steps of current. We recorded from the large calyceal endings as a way to access these
1518 dimorphic afferents, which, like most LES afferents, made contact with both type I and
1519 type II HCs. For current steps (bottom) at 3 × I_{thresh} (×3, green), both genotypes produced
1520 sustained firing, considered typical of regular afferents innervating LES and MES. Here
1521 I_{thresh} (blue trace) was 100 pA for Gpr156$^{del/+}$ afferent and 250 pA for Gpr156$^{del/del}$ afferent,
1522 but overall there was no significant difference in current threshold with genotype.

1523

1524

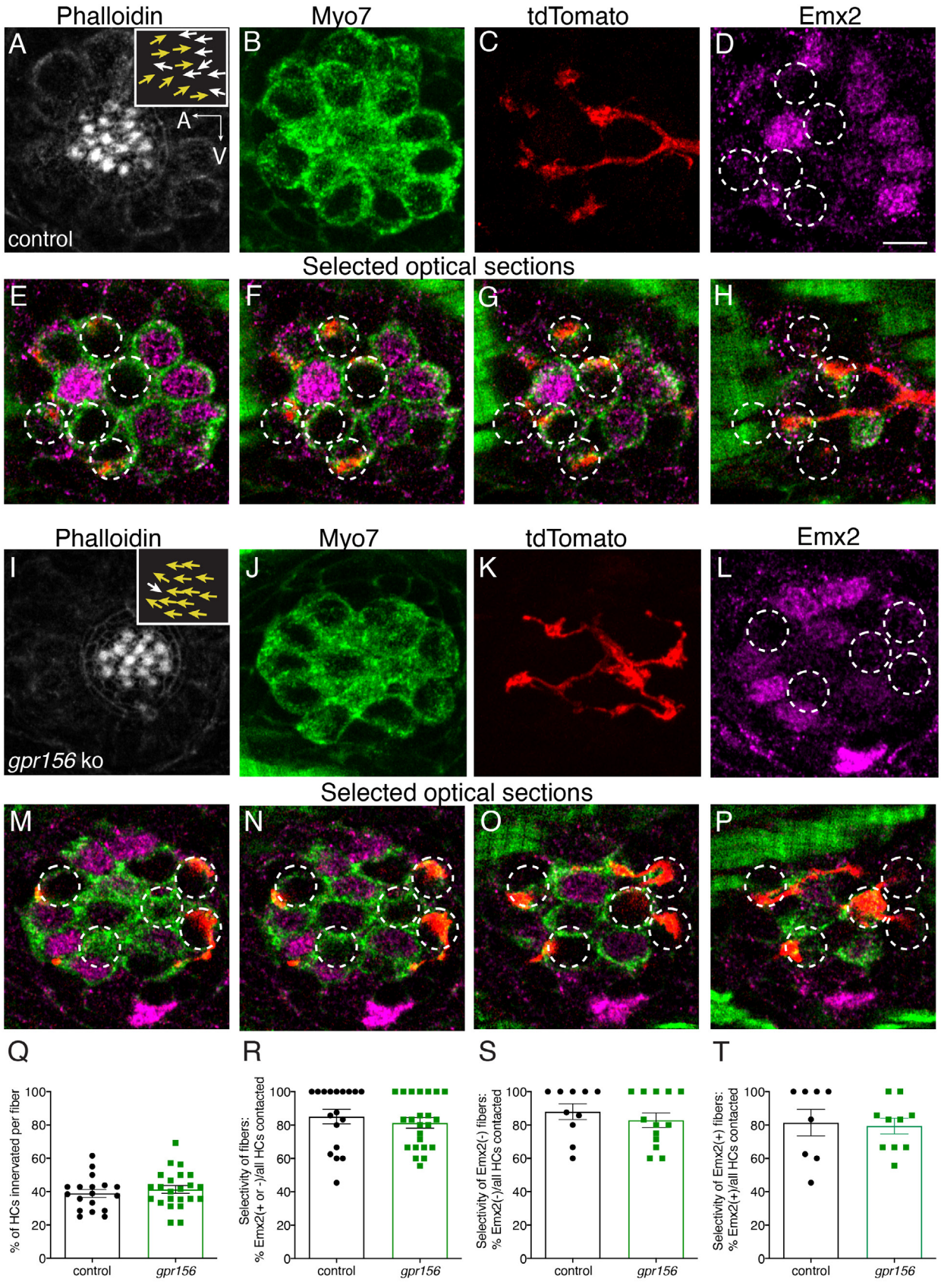
Phalloidin
Myo7
tdTomato
Emx2
A
B
C
D
A
V
control
Selected optical sections
E
F
G
H
Phalloidin
Myo7
tdTomato
Emx2
I
J
K
L
gpr156 ko
Selected optical sections
M
N
O
P
Q
R
S
T
% of HCs innervated per fiber
Selectivity of fibers: % Emx2(+ or -)/all HCs contacted
Selectivity of Emx2(-) fibers: % Emx2(-)/all HCs contacted
Selectivity of Emx2(+) fibers: % Emx2(+)/all HCs contacted
0
20
40
60
80
100
control
gpr156

1525

1526 **Figure 9. Gpr156 was not required for lateral-line afferents to select Emx2^{+} or Emx2^{-}**
1527 **hair cells. A-H**) Images of a control neuromast innervated by a single afferent fiber that
1528 contacts Emx2(-) cells at 5 dpf. **A**) Phalloidin label reveals 16 hair bundles (8 A>P and 8
1529 P>A hair bundles). Z-stack projections show all HCs labeled with Myo7a (**B**) a single
1530 afferent fiber expressing tdTomato (**C)** and Emx2(+ and -) HCs (**D**). **E**-**H**) Selected optical
1531 sections of (**B**–**D**) highlight the single afferent contacting individual Emx2(-) HCs. **I-P**)
1532 Images of a *gpr156* mutant neuromast innervated by a single afferent fiber that contacts
1533 Emx2(-) cells. (**I**) Phalloidin label revealed 14 hair bundles (13 A>P and 1 P>A hair
1534 bundles). Z-stack projections show all HCs labeled with Myo7a (**J**) a single afferent fiber
1535 expressing tdTomato (**K**) and Emx2(+ and -) HCs (**L**). **M-O**) Selected optical sections of
1536 (**J**–**L**) highlight a single afferent in a *gpr156* mutants contacting individual Emx2(-) HCs.
1537 **Q**) In both controls and *gpr156* mutants, each afferent fiber contacted the same number
1538 of HCs per neuromast. **R**) The overall selectivity of afferent fiber for Emx2(+ or -) HCs
1539 were similarly high in *gpr156* mutant and controls. **S**-**T**) The selectivity of afferent fibers
1540 for Emx2(+) or Emx2(-) HCs was similarly high in both *gpr156* mutants and controls.
1541 Arrows in **A** and **I** indicate the orientation of the hair bundles in each example. SEM is
1542 shown in Q-T. An unpaired *t*-test was used for comparisons. Scale bar = 5 μm.
1543

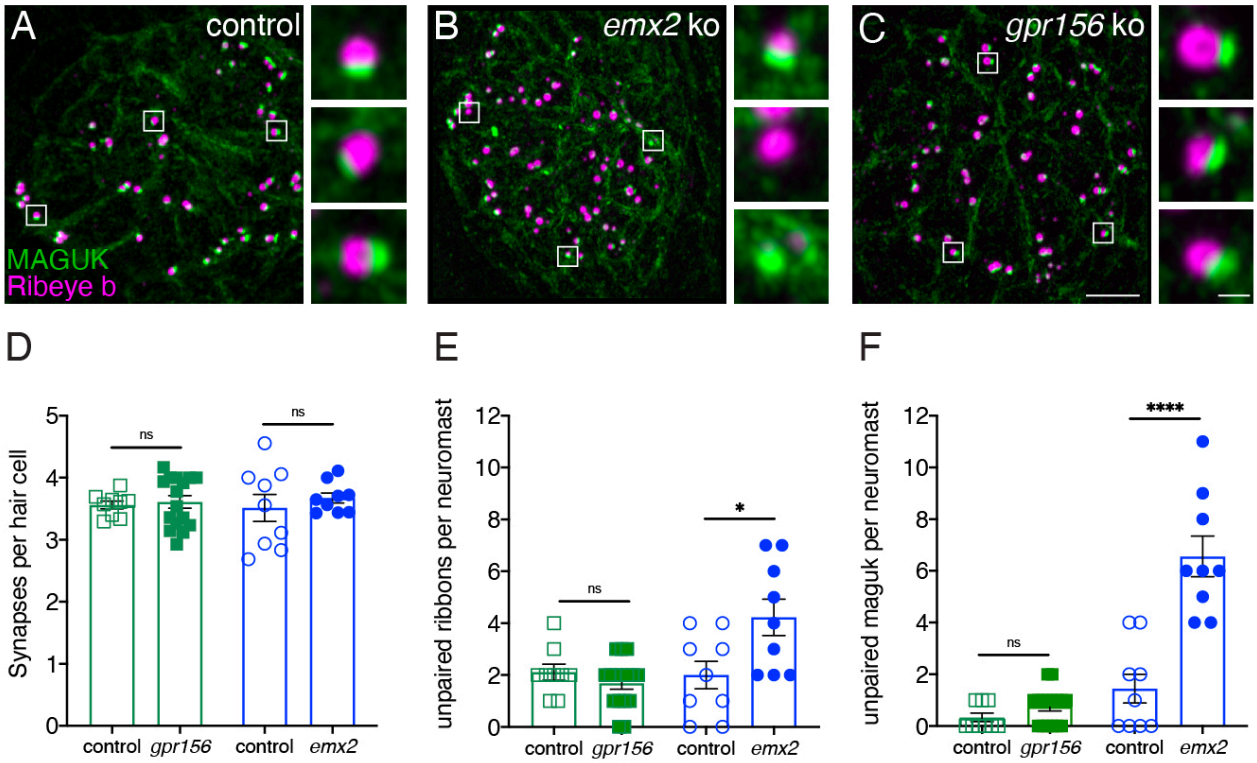

Figure 10. Grp156 was not required for pairing of pre- and post-synapses in lateral-line hair cells. A-C) Images neuromasts immunolabeled with Maguk and Ribeye b to stain HC post- and pre-synapses, respectively at 5 dpf. **A**) Example of an immunostain of a control neuromast showing 3 complete synapses to the right. **B**) Image of an *emx2* mutant neuromast that shows complete synapses, as well as unpaired pre- and postsynapses, shown to the right. **C**) Image of a *gpr156* mutant neuromast, with complete synapses shown to the right. **D**) Quantification revealed the same number of complete synapses per HC in *emx2* and *gpr156* mutants compared to controls. **E-F**) In *gpr156* mutants, quantification revealed there is no difference in the number of unpaired pre- or post-synapses per neuromast compared to controls. In *emx2* mutants, there were significantly more pre- or post-synapses per neuromast compared to controls. SEM is shown in **D-F**. Scale bar = 5 µm. Unpaired t-test were used to make comparisons. *$p < 0.05$, ****$p < 0.0001$.

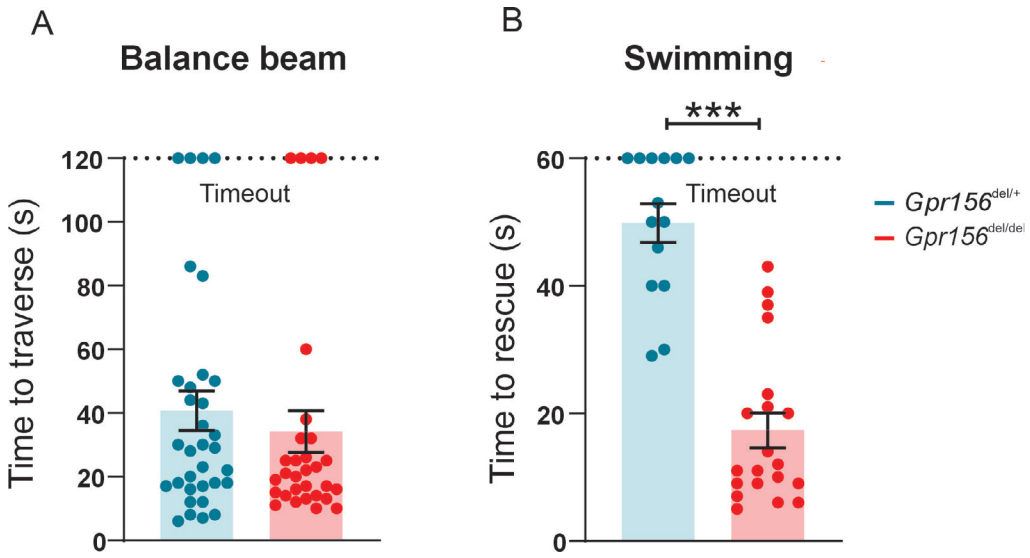

Figure 11. *Gpr156* mutant mice failed to swim and maintain their balance in water. **A**) Time taken to traverse the balance beam for control and *Gpr156*$^{del/del}$ mice. N is 33 and 30 for control (green) and *Gpr156*$^{del/del}$ (red) mice respectively. **B**) Time taken to rescue an animal immediately after the animal exhibited underwater tumbling. N is 14 and 20 for control (green) and *Gpr156*$^{del/del}$ (red) mice respectively. ***P<0.001.

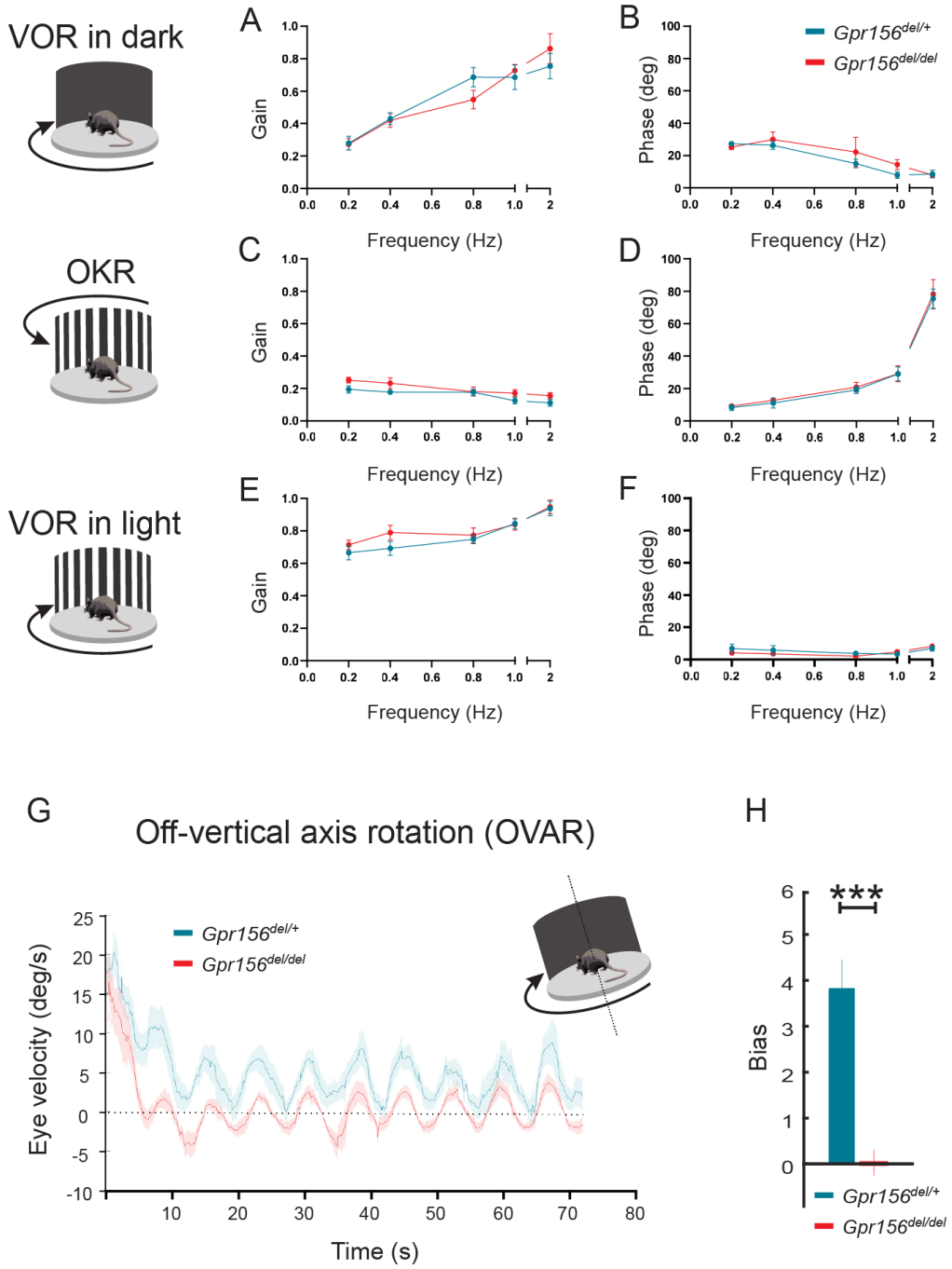

Figure 12. VOR and OKR responses were normal but OVAR responses were altered in *Gpr156*$^{del/del}$ mice. A-B) VORd gain and phase (mean±SEM) plotted as a function of frequency for control and *Gpr156*$^{del/del}$ mice. N is 8 and 7 for control (green) and *Gpr156*$^{del/del}$ KO (red) mice respectively. **C-D**) OKR gain and phase (mean±SEM) plotted as a function of frequency for control and *Gpr156*$^{del/del}$ mice. **E-F)** VORl gain and

1577 phase (mean±SEM) plotted as a function of frequency for control and *Gpr156*$^{del/del}$ mice.
1578 (**G**) Average eye velocities (mean±SEM) during 72s-long off-vertical axis rotation for
1579 control and *Gpr156*$^{del/del}$ mice. N is 8 and 7 for control (green) and *Gpr156*$^{-/-}$ (red) mice
1580 respectively. **H)** OVAR bias during the steady state (mean±SEM) for control and
1581 *Gpr156*$^{del/del}$ mice. ***P<0.001.
1582
1583
1584
1585
1586
1587
1588
1589
1590
1591
1592
1593
1594
1595

TABLES

Table 1. Percent of LES HCs with transduction

	Type I	Type II	ALL
Gpr156 $^{del/+}$	16/22 (73%)	23/38 (60%)	39/60 (65%)
Gpr156 $^{del/del}$	20/29 (69%)	34/46 (73%)	54/75 (72%)
Age range (median)	P11-44 (P19)	P11-100 (P19)	P11-P100 (P18)
p value	0.99	0.63	0.89

Table 2. Genotype comparisons of transduction and adaptation in LES HCs

				G(X) Boltzmann parameters				*Adaptation component tau at X-1/2*			*Adaptation component extent* at X-1/2*			
HC Type	**Genotype**	**n**	**Age (median)**	G_{max}, nS	10-90% OR, nm	$X_{1/2}$, nm	dx, nm	τ_{VF}, ms (n)	τ_F, ms	τ_S, ms	% decay	% A_{VF} (n)	% A_F	% A_S
Type I	***Gpr156*** $^{del/+}$	8	P8-32 (P18)	3.0 ± 0.4	780 ± 50	240 ± 20	180 ± 10	0.3 ± 0.1 (7) n.d. (1)	5.1 ± 0.6	72 ± 12	54 ± 3	32 ± 5 (7)	32 ± 7	36 ± 5
	Gpr156 $^{del/del}$	5	P8-32 (P20)	2.5 ± 0.1	710 ± 70	230 ± 20	190 ± 30	0.3 ± 0.1	7.9 ± 1.6	112 ± 31	61 ± 3	40 ± 7 (5)	28 ± 7	31 ± 3
	Statistics													
	p value			0.15	0.37	0.7	0.83	0.55	0.15	0.18	0.12	0.34	0.72	0.45
	NS power			0.21	0.13	0.07	0.05	0.09	0.42	0.25	0.34	0.14	0.06	0.11
Type II	***Gpr156*** $^{del/+}$	1	P32	2.5 ± 0.2	670 ± 50	220 ± 10	160 ± 20	0.4	8.8	137	82	20	63	17
		4	P10-100 (P15)					n.d.	9.1 ± 3.1	133 ± 88	73 ± 2	0	57 ± 3	43 ± 3
	Gpr156 $^{del/del}$	1	P22	2.2 ± 0.2	810 ± 50	280 ± 30	160 ± 20	0.52	4.4	47	75	26	41	33
		4	P14-44 (P22)					n.d.	9.9 ± 5.7	117 ± 44	73 ± 7	0	52 ± 11	48 ± 11
	Statistics													
	p value			0.39	0.08	0.27	0.79	n/a	0.91	0.88	0.97	n/a	0.66	0.66
	NS power			0.12	0.43	0.17	0.06	n/a	0.05	0.05	0.05	n/a	0.07	0.07

n.d. = very fast component not detected

n/a not available

1616 **Table 3. Genotype comparisons of electrical properties of Type I and II HCs in**
1617 **LES**
1618

HC type	Genotype	n	Age (median)	C_m, pF	V_{rest}, mV	$V_{1/2}$, mV	Slope factor, mV	R_{in} (MΩ)	G_{max}/C_m, nS/pF
Type I	*Gpr156*$^{del/+}$	9-13	P15-34 (P19)	5.8 ± 0.2	-85 ± 1	-83 ± 1	4.5 ± 0.3	46 ± 3	19 ± 2
	Gpr156$^{del/del}$	11-18	P12-44 (P18)	5.8 ± 0.3	-86 ± 1	-84 ± 1	4.8 ± 0.3	51 ± 3	24 ± 4
	p value			0.84	0.84	0.57	0.53	0.37	0.22
	*NS power			0.05	0.05	0.08	0.09	0.14	0.2
Type II	*Gpr156*$^{del/+}$	24-29	P11-47 (P18)	4.7 ± 0.1	-72 ± 1	-31 ± 1	8.9 ± 0.5	598 ± 35	2.7 ± 0.2
	Gpr156$^{del/del}$	28-29	P12-44 (P17)	4.4 ± 0.1	-73 ± 2	-30 ± 1	9.0 ± 0.6	575 ± 41	3.2 ± 0.2
	p value			0.14	0.71	0.48	0.85	0.67	0.11
	*NS power			0.31	0.07	0.1	0.05	0.07	0.34

1619

1620 *estimated power of non-significant result

1621
1622
1623
1624
1625
1626
1627
1628
1629
1630
1631
1632
1633

1634 **Table 4. Genotype comparison of G(X) and adaptation parameters (all hair cells)**

			G(X) Boltzmann parameters				*Adaptation component tau at $X_{1/2}$*			*Adaptation component extent at $X_{1/2}$*			
Genotype	**n**	**Age (median)**	**G_{max}, nS**	**10-90% OR, nm**	**$X_{1/2}$, nm**	**dx, nm**	**τ_{VF}, ms (n)**	**τ_F, ms**	**τ_S, ms**	**% decay**	**% A_{VF} (n)**	**% A_F**	**% A_S**
Gpr156 $^{del/+}$	23	P8-32 (P18)	3.0 ± 0.2	660 ± 40	200 ± 10	160 ± 10	0.3 ± 0.1 (14) n.d. (9)	10.5 ± 1.8	152 ± 31	64 ± 2	24 ± 5 (14) n.d. (9)	39 ± 4	37 ± 3
Gpr156 $^{del/del}$	26	P8-32 (P20)	2.9 ± 0.2	720 ± 40	250 ± 20	160 ± 10	0.3 ± 0.3 (14) n.d. (12)	7.8 ± 1.0	140 ± 21	68 ± 3	24 ± 5 (14) n.d (12)	36 ± 4	40 ± 4
Statistics													
p value			0.91	0.26	0.11	0.9	0.44	0.18	0.75	0.3	0.95	0.67	0.62
NS power			0.05	0.2	0.36	0.05	0.12	0.27	0.06	0.18	0.05	0.07	0.08

1635
1636 Includes both cell types and all zones
1637 n.d. = very fast component not detected
1638
1639
1640
1641
1642

1643 **Table 5. Genotype comparison of excitability in LES afferents**

1644

Genotype	n	Age range (median)	# Transient	# Sustained	V_{rest}, mV	R_{in}, MΩ	I-threshold, pA
Gpr156 $^{del/+}$	18	P11-35 (P19)	1 (5%)	17 (94.5%)	-66 ± 1	614 ± 145	111 ± 27
Gpr156 $^{del/del}$	20	P13-35 (P16)	1 (5.0%)	19 (95.0%)	-67 ± 1	323 ± 67	105 ± 20
Statistics							
p value				0.99	0.20	0.09	0.85
***NS power**					0.25	0.43	0.05

1645

1646 *estimated power of non-significant result

1647

1648 **Supplemental Figures**

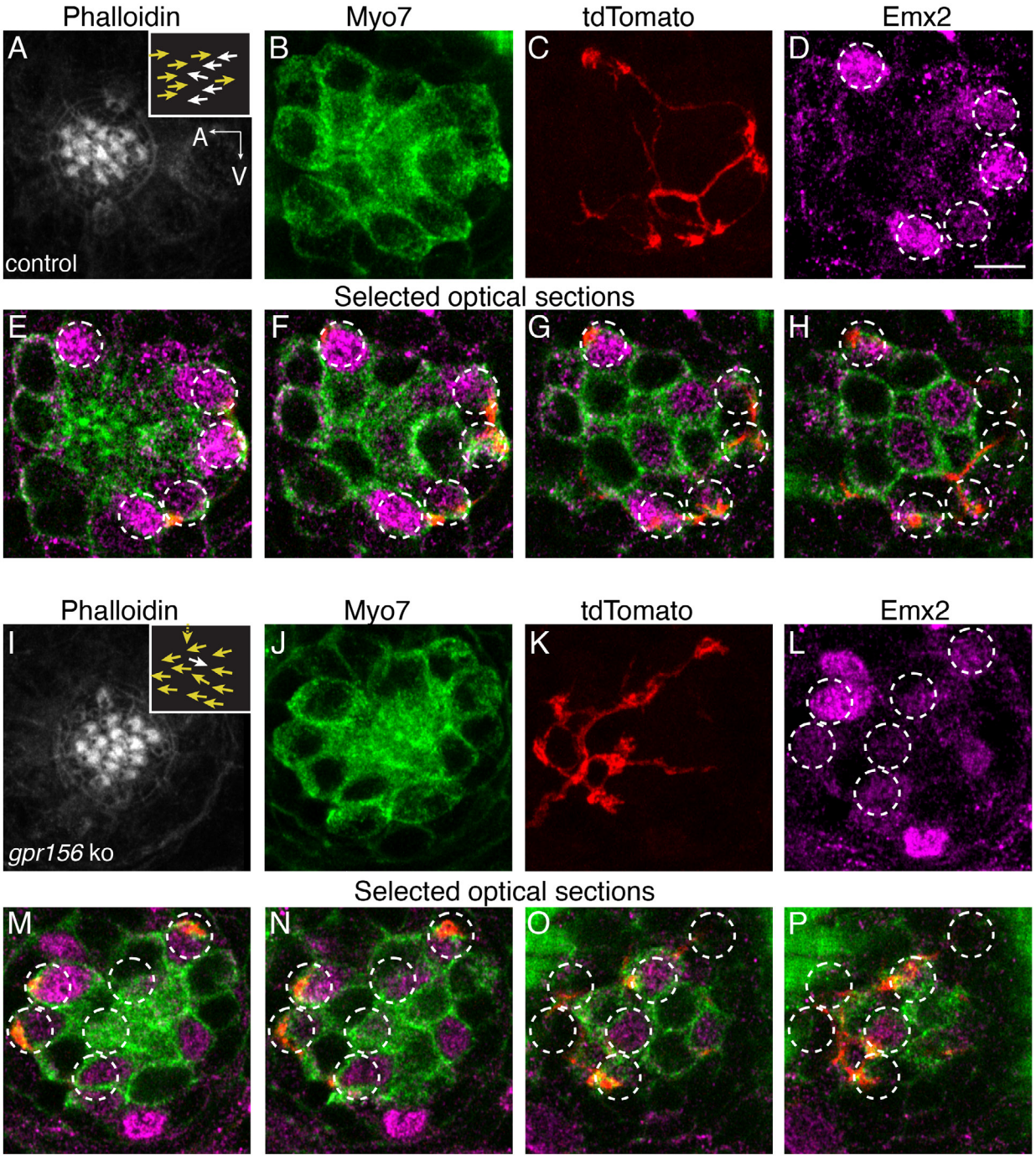

1649

1650

1651 **Supplemental figure 1. Gpr156 was not required for lateral-line afferents to select**
1652 **Emx2⁺ HCs. A-H)** Images of a control neuromast innervated by a single afferent fiber that
1653 contacts Emx2⁺ cells. (A) Phalloidin label reveals 14 hair bundles (7 A>P and 7 P>A hair
1654 bundles). Z-stack projections show all HCs labeled with Myo7a (**B**) a single afferent fiber
1655 expressing tdTomato (**C**) and Emx2⁺ and Emx2⁻ HCs (**D**). (**E-H**) Selected optical sections

1656 of (**B**–**D**) highlight the single afferent contacting individual Emx2$^+$ HCs. (**I**-**P**) Images of a
1657 *gpr156* mutant neuromast innervated by a single afferent fiber that contacts Emx2$^+$ cells.
1658 **I**) Phalloidin label revealed 14 hair bundles (12 A>P and 1 P>A hair bundles, 1 at 90°). Z-
1659 stack projections show all HCs labeled with Myo7a (**J**) a single afferent fiber expressing
1660 tdTomato (**K**) and Emx2$^+$ and Emx2$^-$ HCs (**L**). **M**-**O**) Selected optical sections of (**J**–**L**)
1661 highlight a single afferent in a *gpr156* mutants contacting individual Emx2$^+$ HCs. Arrows
1662 in **A** and **I** indicate the orientation of the hair bundles in each example. Scale bar: 5 μm.
1663

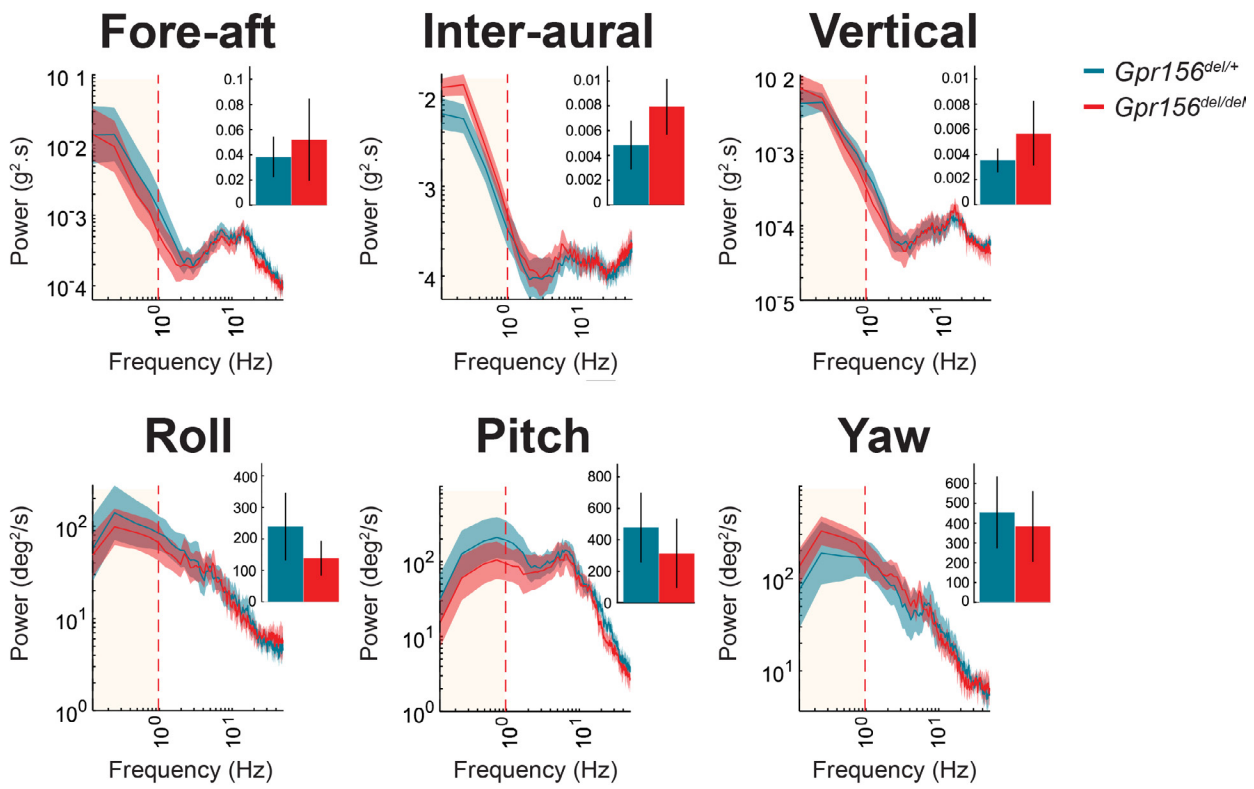

Supplemental figure 2. No resting head tremor was observed in *Gpr156*$^{del/del}$ mice. Comparison of power spectra density of head movements at rest in translational axes and rotational axes between control and *Gpr156*$^{del/del}$. N is 8 and 7 for control and *Gpr156*$^{del/del}$ mice respectively. Error bars: SEM.

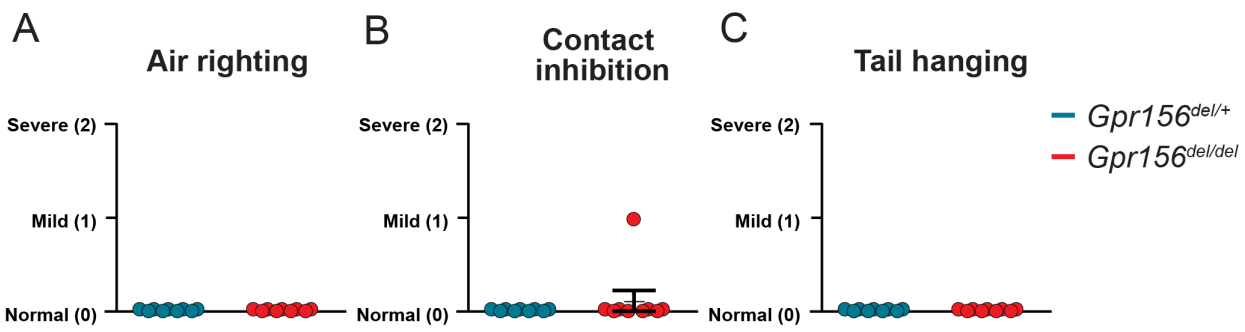

Supplemental figure 3. *Gpr156*$^{del/del}$ mice scored normally on several basic standard behavioral tests. Comparison of assigned scores between *Gpr156*$^{del/del}$ and control mice show no impairment in (**A**) air righting, (**B**) contact inhibition, (**C**) tail hanging. N is 9 and 7 for control and *Gpr156*$^{del/del}$ mice respectively. Error bars: SEM.

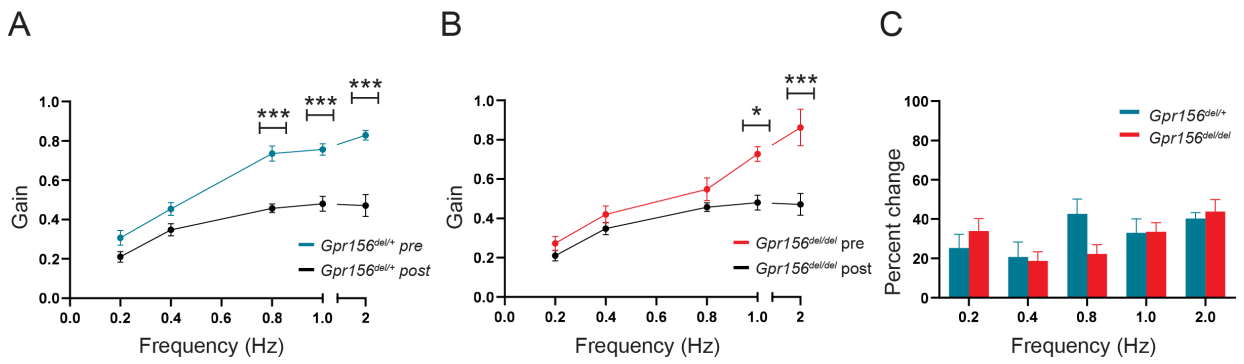

Supplemental figure 4. VOR learning was unimpaired in *Gpr156*$^{del/del}$ mice. A) VORd gain (mean ± SEM) before and after the VOR gain-down training plotted as a function of frequency for control mice (N = 7). **B**) VORd gain (mean ± SEM) before and after the VOR gain-down training plotted as a function of frequency for *Gpr156*$^{del/del}$ mice (N = 7). **C**) Percent change in VOR gain for control and *Gpr156*$^{del/del}$. *P<0.05, ***P<0.001.